metals

MDPI

Article

Selective Laser Melting of Multi-Material Ti15Ta/Ti6Al4V Structures for Biomedical Applications: From Process Parameters to Mechanical Properties and Biological Response

Igor Polozov *, Victoria Nefyodova, Anton Zolotarev, Victoria Sokolova, Sergey Chibrikov and Anatoly Popovich

Institute of Machinery, Materials, and Transport, Peter the Great St. Petersburg Polytechnic University (SPbPU), Polytechnicheskaya, 29, 195251 St. Petersburg, Russia; nefedova_va@spbstu.ru (V.N.); zolotarev_am@spbstu.ru (A.Z.); sokolova_vv@spbstu.ru (V.S.); chibrikov.sk@edu.spbstu.ru (S.C.); director@immet.spbstu.ru (A.P.)

* Correspondence: polozov_ia@spbstu.ru

Abstract

Multi-material structures based on titanium alloys represent a promising approach for the fabrication of functionally graded orthopedic implants capable of combining high mechanical strength with reduced stiffness to minimize the stress-shielding effect. In the present work, multi-material Ti15Ta/Ti6Al4V specimens were fabricated by laser powder bed fusion (L-PBF) for the first time, and the processing parameters of the transition zone were systematically optimized. Three regimes were investigated: baseline (93 J/mm^3), double scanning (186 J/mm^3), and reduced speed (116 J/mm^3). The microstructure and elemental distribution were examined by SEM and EDS; mechanical properties were evaluated through tensile testing and microhardness measurements; biocompatibility was assessed using osteoblasts and gingival fibroblasts. The double scanning regime provided the highest density of the transition zone (99.49%). Tensile failure of the specimens occurred in the Ti15Ta region, confirming the quality of the metallurgical bond. The ultimate tensile strength ranged from 534 to 543 MPa with an elongation at break of 15.7–16.4%. Heat treatment at 875 °C led to the formation of an equilibrium lamellar microstructure and smoothing of the interface. Cell viability on both alloys exceeded 88% as confirmed by flow cytometry and remained above the 70% non-cytotoxicity threshold defined by ISO 10993-5. The obtained results demonstrate the technological feasibility of fabricating multi-material Ti15Ta/Ti6Al4V structures and achieving high-quality metallurgical bonding, which constitutes a necessary first step toward the development of functionally graded orthopedic implants.

Keywords: laser powder bed fusion; multi-material structures; titanium alloys; Ti15Ta; Ti6Al4V; functionally graded materials; transition zone; biocompatibility; orthopedic implants

Check for updates

Academic Editors: Chao Yu and Hong Xiao

Received: 6 February 2026
Revised: 25 February 2026
Accepted: 5 March 2026
Published: 8 March 2026

Copyright: © 2026 by the authors. Licensee MDPI, Basel, Switzerland. This article is an open access article distributed under the terms and conditions of the Creative Commons Attribution (CC BY) license.

1. Introduction

Titanium and its alloys are widely used in orthopedics owing to their combination of high specific strength, corrosion resistance, and biocompatibility [1]. Among these, the Ti-6Al-4V alloy has become the gold standard for load-bearing implants [2]. This α + β alloy possesses excellent mechanical properties: an ultimate tensile strength of 895–1170 MPa and high fatigue strength [3]. However, Ti6Al4V has two significant drawbacks that limit the long-term performance of implants.

The first problem is related to the cytotoxicity of vanadium and aluminum ions released during the degradation of Ti6Al4V. Studies have shown that these ions exhibit cytotoxic effects on osteoblasts and fibroblasts, with vanadium being released more rapidly than titanium and aluminum [4,5]. In vivo experiments have demonstrated that Ti6Al4V particles can induce pathological tissue reactions, while aluminum and vanadium may potentially contribute to neurological complications [6,7]. These findings have stimulated the search for alternative titanium alloys incorporating biocompatible elements (Ta, Nb, Zr, Mo) [8].

The second problem is associated with the stress-shielding effect, which arises from the mismatch between the elastic moduli of Ti6Al4V (105–120 GPa) and human cortical bone (10–30 GPa) [9]. This mechanical incompatibility leads to improper stress distribution: the implant bears the majority of the load, while the surrounding bone experiences insufficient mechanical stimulation [10]. According to Wolff's law, chronic stress insufficiency triggers adaptive bone remodeling, leading to a loss of bone density. The subsequent resorption and weakening of the bone result in aseptic loosening—the primary cause of revision surgeries in total hip arthroplasty.

To address these problems, new titanium alloys with a reduced elastic modulus composed of non-toxic elements are being actively developed [8]. Binary Ti-Ta alloys are of particular interest. Early studies have shown that alloys with up to 50 wt.% Ta achieve a reduction in the elastic modulus while maintaining mechanical strength [11–15]. In one study employing selective laser melting, a Ti-15Ta-xZr alloy was produced, achieving an elastic modulus of 43 GPa—close to that of cortical bone—with a strength exceeding 900 MPa [15].

The concept of functionally graded materials (FGM) offers a novel solution for simultaneously ensuring mechanical compatibility and structural strength of orthopedic implants. It may allow combining the advantages of Ti6Al4V and Ti-Ta within a single implant. Unlike homogeneous materials, FGM implants are characterized by spatially varying composition and properties within a single component, enabling the optimization of characteristics for different zones with distinct mechanical requirements [16–18]. For total hip endoprostheses, this approach is particularly advantageous: the femoral neck region requires high fatigue strength to withstand cyclic loads during walking, whereas the zone in contact with trabecular bone necessitates reduced stiffness to minimize stress shielding.

From a structural design standpoint, the optimal configuration of a dual-alloy femoral stem involves a Ti6Al4V core extending through the neck and distal portion of the stem, where maximum strength and stiffness are required, with Ti15Ta forming the outer surface of the implant. Such an architecture ensures direct contact of the Ti15Ta layer with trabecular bone, reducing the stress-shielding effect, while the internal Ti6Al4V skeleton maintains the structural integrity necessary to prevent implant failure.

Additive manufacturing, in particular laser powder bed fusion (L-PBF, also known as selective laser melting, SLM), is one of the technologies for fabricating multi-material components [19–21]. Unlike conventional casting, forging, and machining methods, L-PBF builds parts layer by layer through selective melting of metal powder, providing design freedom and the ability to create patient-specific geometries [22]. The layer-by-layer nature of the process is also ideal for multi-material manufacturing: sequential deposition of different powders creates compositional gradients unattainable by conventional methods. For titanium alloys, L-PBF has demonstrated the capability to produce parts with mechanical properties equal to or exceeding those of conventionally manufactured components [23,24].

However, multi-material L-PBF is associated with significant technological challenges. The transition zone is a critical region: each alloy has its own optimal processing parameters (laser power, scanning speed, energy density), determined by thermophysical properties—melting temperature, thermal conductivity, and absorptivity [25]. Parameter

mismatch leads to defects: porosity (incomplete melting, gas entrapment), lack of fusion (insufficient energy), hot cracking (solidification under stress), and delamination at the interface [26–28]. A systematic review by NIST [29] classifies L-PBF defects: gas porosity up to 0.7%, with lack-of-fusion defects critically affecting fatigue performance. Thermal stresses exacerbate the problem: differences in the coefficients of thermal expansion and thermal conductivity between Ti-Ta and Ti6Al4V induce residual stress concentrations and microcracks at the interface.

Successful multi-material L-PBF has been demonstrated for the Ti-6Al-4V/Ti-6Al-2Sn-4Zr-2Mo system, where defect-free interfaces with high-quality metallurgical bonding were achieved; however, these alloys have similar chemical compositions and comparable thermophysical properties [30]. The Ti-Ta/Ti-6Al-4V combination presents different conditions: the binary Ti-Ta phase diagram exhibits complete mutual solubility of the components with the formation of continuous solid solutions across the entire concentration range, which theoretically promotes the formation of a strong metallurgical bond; however, the substantial compositional gradient and differences in thermophysical properties necessitate the development of specialized processing strategies for the transition zone. The study by Danlei Zhao et al. [31] demonstrated the achievement of elastic moduli of 89 GPa with an ultimate tensile strength exceeding 1000 MPa, confirming the processability of Ti-Ta compositions by laser powder bed fusion. Nevertheless, systematic literature reviews on multi-material L-PBF [32] reveal a research gap: despite growing interest in multi-material additive manufacturing and the successful application of L-PBF for both Ti6Al4V and Ti-Ta alloys individually, studies on multi-material joining of Ti-Ta with Ti6Al4V are virtually absent.

To contextualize the present work within the existing body of research, Table 1 summarizes previously reported multi-material titanium systems fabricated by L-PBF.

Table 1. Summary of previously reported multi-material titanium systems fabricated by L-PBF.

Material Combination	Process Strategy	Key Achieved Properties	Limitations	References
CP-Ti/Ti6Al4V	L-PBF, sequential deposition, different graded zone geometries	Defect-free transition zone; effects of heat treatment and HIP investigated	Both materials possess high elastic modulus; does not address stress shielding; no biocompatibility assessment	[33]
NiTi/Ti6Al4V	L-PBF, multi-material cellular structures	Cellular structures for orthopedic implants combining NiTi superelasticity with Ti6Al4V strength	Formation of brittle intermetallics (Ti_2Ni) at the interface; Ni cytotoxicity; limited ductility	[34]
Ti6Al4V/Ti-6Al-2Sn-4Zr-2Mo	L-PBF, sequential deposition	Defect-free interface; UTS = 1314 MPa	Similar chemistry and thermophysical properties; no elastic modulus reduction; low elongation (2.8%); aerospace application	[30]
Ti6Al4V/γ-TiAl	L-PBF, sequential deposition	Gradient interface ~250 µm achieved	Fabrication failed due to cold cracking of γ-TiAl; not suitable for biomedical applications	[30]
Ti6Al4V/Al-Cu-Mg	L-PBF, Cu interlayer	Crack suppression via Cu interlayer; multi-material lattice structures	Vastly different thermophysical properties; Cu interlayer required; not intended for biomedical use	[35]
Ti→Ta (gradient)	L-PBF, horizontal and vertical compositional grading	Semi-continuous Ti-to-Ta compositional gradient demonstrated	No systematic evaluation of mechanical properties or biocompatibility; proof-of-concept only	[36]

As shown in Table 1, previously reported multi-material titanium systems fabricated by L-PBF have been limited to alloy combinations with similar chemical compositions (e.g., CP-Ti/Ti6Al4V), systems containing cytotoxic elements (e.g., NiTi/Ti6Al4V), or combinations not intended for biomedical applications (e.g., Ti6Al4V/Al-Cu-Mg). Although a Ti-to-Ta compositional gradient has been demonstrated as a proof of concept [36], no study has systematically investigated multi-material L-PBF structures combining a biocompati-

ble Ti-Ta alloy with Ti6Al4V, including transition zone optimization, mechanical testing, and biocompatibility assessment. The Ti15Ta/Ti6Al4V combination investigated in the present work addresses this gap by pairing a high-strength α + β alloy (Ti6Al4V) with a low-modulus binary alloy (Ti15Ta) containing biocompatible alloying elements, thereby potentially targeting the stress-shielding effect and cytotoxicity concerns associated with conventional Ti6Al4V implants.

The aim of this study is the development and optimization of L-PBF strategies for the fabrication of Ti15Ta/Ti6Al4V multi-material structures with high-quality transition zones for biomedical implants. The objectives of this work are: (1) establishing optimal process parameters for the transition zone that minimize porosity and prevent defects; (2) characterization of the microstructure across the interface (phase composition, grain morphology, elemental distribution); (3) evaluation of mechanical properties (microhardness, tensile strength); (4) investigation of the effect of heat treatment on the microstructure and properties of the transition zone; (5) in vitro biocompatibility assessment. This study addresses the gap in multi-material additive manufacturing of titanium alloys and establishes a scientific foundation for next-generation functionally graded orthopedic implants.

2. Materials and Methods

2.1. Powder Characteristics

In the present study, Ti15Ta (wt.%) and Ti-6Al-4V (wt.%) alloy powders were used as feedstock materials. The Ti15Ta powder was supplied by Guangzhou Sailong Additive Manufacturing Co., Ltd. (Guangzhou, China). The powder particles exhibit a spherical morphology characteristic of materials produced by gas atomization (Figure 1a). Particle size analysis performed using a Fritsch Analysette 22 NanoTec plus laser particle size analyzer (Fritsch GmbH, Idar-Oberstein, Germany) revealed a relatively narrow size distribution: d10 = 14 μm, d50 = 35.2 μm, and d90 = 68.7 μm. The Ti-6Al-4V alloy powder (Normin LLC, Borovichi, Russia) was produced by plasma atomization with the following particle size distribution: d10 = 40.3 μm, d50 = 67 μm, and d90 = 105.3 μm. The powder particles exhibit a spherical morphology (Figure 1b). SEM examination (Figure 1a,b) revealed a fine dendritic surface structure typical of rapid solidification. The distribution plots (Figure 1c,d) confirm a normal particle size distribution with a minimal presence of satellites, ensuring good flowability during the L-PBF process.

2.2. L-PBF Process Parameters

Specimens were fabricated using a 3DLam MINI selective laser melting system (3DLam, Saint Petersburg, Russia) equipped with an IPG Photonics fiber laser (IPG Photonics, Marlborough, MA, USA) with a maximum power of 300 W and a beam diameter of 70 μm. The process was conducted under a high-purity argon atmosphere (O_2 < 100 ppm) on a titanium build platform. The scanning strategy comprised linear scanning with a 90° rotation between layers. The dimensions of the fabricated specimens were 10 mm × 5 mm × 10 mm, with three specimens per regime.

Multi-material specimens were fabricated layer by layer in the following sequence (Figure 2). Ti6Al4V alloy was used as the base material and was printed directly onto the titanium build platform. Upon completion of the lower portion of the specimen with a height of 5 mm, the process was paused for powder changeover. The material changeover procedure included: removal of residual Ti6Al4V powder from the build chamber using a vacuum cleaner, cleaning of the chamber surfaces with isopropyl alcohol-soaked wipes, and loading of Ti15Ta powder into the feed hopper. Following the powder changeover, the chamber was purged with high-purity argon until the oxygen content fell below 100 ppm.

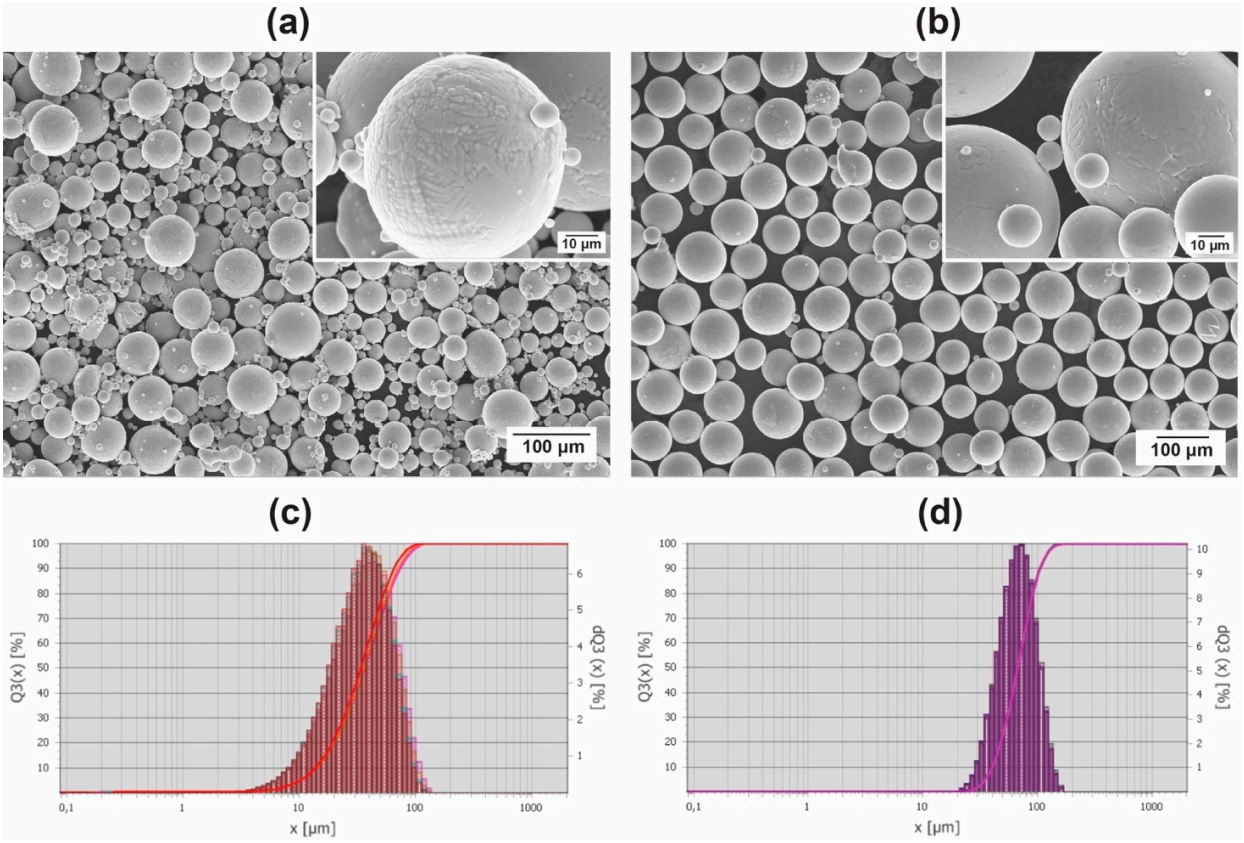


Figure 1. Characterization of Ti15Ta and Ti6Al4V powders: (**a**) scanning electron microscopy (SEM) micrographs of Ti15Ta powder showing the overall particle morphology and high-magnification view of individual particle surfaces; (**b**) scanning electron microscopy (SEM) micrographs of Ti6Al4V powder showing the overall particle morphology and high-magnification view of individual particle surfaces; (**c**) particle size distribution histogram with differential curve for Ti15Ta powder; (**d**) particle size distribution histogram with differential curve for Ti6Al4V powder.

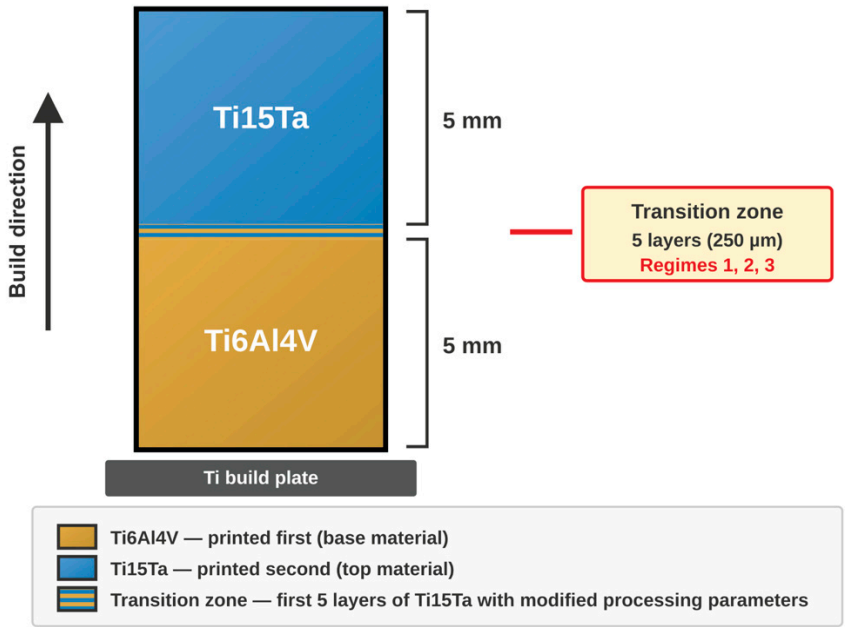


Figure 2. Schematic of the Ti15Ta/Ti6Al4V multi-material sample architecture.

Printing of the upper portion of the specimen from Ti15Ta alloy commenced directly on the surface of the solidified Ti6Al4V. The first five layers of Ti15Ta (with a cumula-

tive thickness of 250 μm) constituted the transition zone, for which various processing regimes were investigated (Table 2). The remaining Ti15Ta layers were printed using the baseline parameters.

Table 2. Printing parameters for the transition zone.

Regime	Power (P), W	Speed (V), mm/s	Layer Thickness (t), μm	h, μm	Double Scanning	Energy Density, J/mm^3	Scanning Strategy
1	280	600	50	100	No	93	Linear with 90° rotation
2	280	600	50	100	Yes	186	Linear with 90° rotation
3	280	480	50	100	No	116	Linear with 90° rotation

Based on our previous studies on the optimization of the Ti15Ta alloy and literature data on Ti6Al4V processing parameters [37,38], it was established that the optimal L-PBF regimes for Ti15Ta and Ti6Al4V alloys are quite similar. Consequently, in order to minimize thermal stresses at the interface and ensure metallurgical compatibility between the two materials, a unified set of processing parameters was applied for both alloys: laser power of 280 W, scanning speed of 600 mm/s, layer thickness of 50 μm, hatch spacing of 100 μm, yielding a volumetric energy density of 93 J/mm^3, with a linear scanning strategy and 90° rotation between layers. Additionally, to investigate the effect of printing parameters on the properties of the transition zone, two modified strategies with increased energy density were implemented for the first five transition layers. Table 2 presents the different regimes for the transition zone: Regime 1—baseline, with parameters identical to those of the bulk materials; Regime 2—a regime employing double scanning; Regime 3—a regime with the scanning speed reduced by 20%.

The volumetric energy density (E, J/mm^3) was calculated using the following equation:

$$E = \frac{P}{v \cdot h \cdot t}, \quad (1)$$

where P is laser power (W), v is scanning speed (mm/s), h is hatch spacing (μm), and t is layer thickness (μm).

2.3. Heat Treatment

Multi-material specimens consisting of Ti15Ta and Ti6Al4V alloys were subjected to heat treatment under the following conditions: vacuum annealing at 875 °C for 2 h followed by furnace cooling. The specimens were heated at a rate of 10 °C/min to the target temperature in a vacuum furnace (Carbolite Gero, Hope Valley, UK) at a vacuum level of 10^{-5} mbar.

The annealing temperature of 875 °C was selected as a compromise for the Ti15Ta/Ti6Al4V multi-material system, ensuring that the Ti6Al4V alloy remains within the two-phase (α + β) region (β-transus~995 °C) while the Ti15Ta alloy is partially or fully within the β-phase region (β-transus~860 °C). This temperature promotes complete recrystallization of the microstructure after additive manufacturing while minimizing grain growth.

2.4. Characterization Methods

2.4.1. Porosity Evaluation

The relative density of the specimens was determined by examining polished cross-sections during metallographic analysis using a Leica DMi 8 optical microscope (Leica, Wetzlar, Germany) equipped with a digital camera. Cross-sectional specimens were prepared in accordance with standard metallographic protocols. Porosity was evaluated using ImageJ (version 1.54g) software by analyzing the transition zone area. The relative density

was calculated as follows: the pore area was subtracted from the total cross-sectional area, and the result was divided by the total cross-sectional area.

2.4.2. Microstructural Analysis

Specimens for microstructural analysis were prepared using standard metallographic procedures. The specimens were sequentially ground on abrasive paper with grit sizes ranging from 240 to 1200, followed by polishing with a 0.05 µm diamond suspension with the addition of hydrogen peroxide. To reveal microstructural features, the polished specimens were etched with Kroll's reagent (2 mL HF, 6 mL HNO_3, and 92 mL H_2O) for 15–20 s at room temperature.

Microstructural examination was performed using a scanning electron microscope (MIRA 3, TESCAN, Brno, Czech Republic) equipped with an energy-dispersive spectrometer (EDS) for elemental analysis. Imaging was carried out at accelerating voltages of 15 to 20 kV using secondary electron and backscattered electron detectors to optimize contrast between different phases.

2.4.3. Mechanical Testing

Vickers microhardness measurements were performed using a hardness tester (Wilson VH1202, Buehler, Lake Bluff, IL, USA) at a load of 300 g (HV0.3) with a dwell time of 15 s. The following measurement strategy was developed to investigate the microhardness distribution in the transition zone (Figure 3a). The transition boundary between the Ti15Ta and Ti6Al4V alloys was identified visually by optical microscopy. Measurements were taken perpendicular to the transition line at 200 µm intervals in both directions from the interface. The selected spacing between indentations satisfies the requirement that the distance between adjacent measurements must be at least three times the indenter imprint diameter, thereby eliminating the influence of deformed zones on the measurement results. To ensure statistical reliability, measurements were conducted along six parallel lines spaced 200 µm apart. The measurement points on adjacent lines were offset by 100 µm relative to one another along the Y-axis to obtain a more detailed map of the hardness distribution in the transition zone.

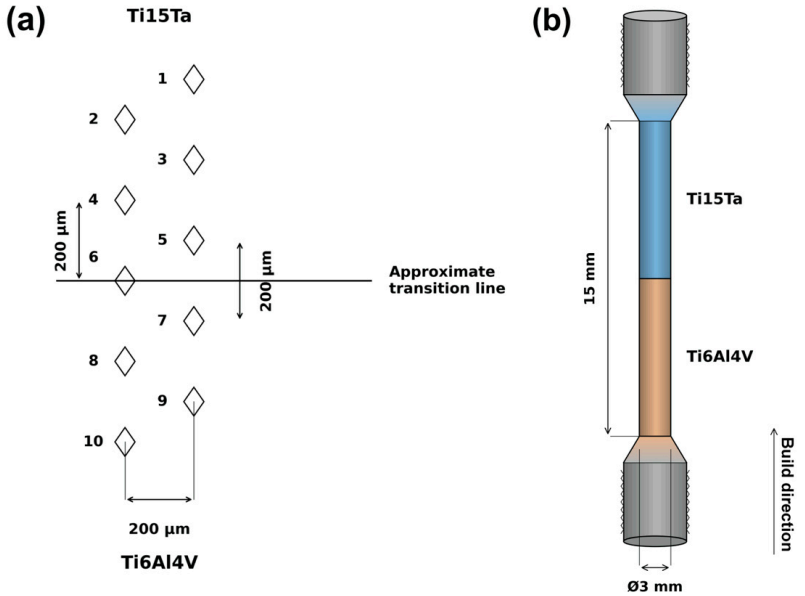


Figure 3. Schematic representation of mechanical testing procedures for Ti15Ta/Ti6Al4V multi-material samples: (**a**) microhardness measurement layout across the transition zone; (**b**) geometry of the tensile specimen.

Tensile tests were performed on a universal testing machine (Zwick/Roell Z100, ZwickRoell GmbH & Co., Ulm, Germany) at room temperature at a strain rate of 0.001 s^{-1} in accordance with the ASTM E8/E8M standard [39]. Multi-material specimens consisting of two parts were used: one half of the specimen was a Ti15Ta alloy and the other half was a Ti6Al4V alloy (Figure 3b). The tensile specimens were machined from as-built L-PBF blocks by turning on a lathe to achieve the final cylindrical geometry. The specimen dimensions were as follows: a gauge length of 15 mm, a parallel length of 17 mm, and a gauge diameter of 3 mm. No additional surface polishing was performed after machining. A minimum of three specimens per processing regime were tested to ensure reproducibility of the results. The elastic modulus was determined using an extensometer attached to the gauge section of the specimen during the initial loading stage.

2.4.4. Evaluation of the Biological Response to Titanium Alloys

For biological studies, specimens with dimensions of 10 mm × 10 mm × 5 mm were prepared. The surfaces were ground on abrasive paper to a grit size of 1200.

Cell Culture

Primary human osteoblasts were isolated from femur bone explants at the Institute of Cytology of the Russian Academy of Sciences (St. Petersburg, Russia) according to the previously described protocol [40]. Human gingival fibroblasts were purchased from the Pokrovsky Stem Cell Bank (St. Petersburg, Russia).

Human osteoblasts and gingival fibroblasts were used as cell models to evaluate the biological response to Ti15Ta and Ti6Al4V alloys produced by selective laser melting. Osteoblasts were cultured in Dulbecco's Modified Eagle Medium with high glucose content (DMEM 4.5 g/L, Gibco, Thermo Fisher Scientific, Waltham, MA, USA) supplemented with 10% fetal bovine serum (FBS, HyClone, Cytiva, Waltham, MA, USA), 1% penicillin-streptomycin solution (Gibco, Thermo Fisher Scientific, Waltham, MA, USA), 1% L-glutamine (Gibco, Thermo Fisher Scientific, Waltham, MA, USA), and 50 μg/mL ascorbic acid. Gingival fibroblasts were cultured in low-glucose DMEM (1.0 g/L, Gibco, Thermo Fisher Scientific, Waltham, MA, USA) with the same supplements except for ascorbic acid. All cultures were incubated at 37 °C in a 5% CO_2 atmosphere.

Scanning Electron Microscopy

To assess cell morphology and cell–surface interactions, osteoblasts and gingival fibroblasts were seeded onto pre-sterilized titanium substrates at a density of 5×10^4 cells per specimen in 48-well plates. Culturing was performed in the respective culture media at 37 °C and 5% CO_2. After 120 h of incubation, specimens with cells were washed with phosphate-buffered saline (PBS) and fixed with 2.5% glutaraldehyde solution for 1 h at 4 °C. The specimens were then washed again with PBS and dehydrated through a graded ethanol series of increasing concentration (30%, 50%, 70%, 80%, 90%, 100%). Following dehydration, the specimens were air-dried and sputter-coated with gold. The prepared specimens were analyzed using a JSM-7001F scanning electron microscope (JEOL, Akishima, Tokyo, Japan).

MTT Assay

Cytotoxicity was evaluated using the MTT assay (3-(4,5-dimethylthiazol-2-yl)-2,5-diphenyltetrazolium bromide, Service Bio, China). Cells were seeded at a density of 5×10^4 onto pre-sterilized titanium substrates in 48-well plates. Cells cultured on tissue culture plastic coated with 0.2% gelatin served as controls. Assessments were performed at 48 and 120 h of culture.

To exclude the contribution of cells attached to the plastic, substrates with cells were transferred to new wells prior to the addition of MTT reagent (100 μL per well). After 2 h

of incubation at 37 °C, formazan crystals were dissolved in 100 µL of DMSO (Biolot, Saint Petersburg, Russia). Optical density was measured at a wavelength of 570 nm (reference wavelength 620 nm). Viability was calculated as a percentage of the control, normalized to the substrate area. A minimum of five replicates per condition were used.

Flow Cytometry

Cell viability was quantitatively assessed by flow cytometry with propidium iodide (PI) staining. Cells (5×10^4) were cultured on titanium substrates for 120 h, after which the substrates were transferred to new wells to exclude cells from the plastic surface.

Cells were detached using 5% trypsin solution (Gibco, USA), centrifuged (300 *g*, 5 min), resuspended in 100 µL of FBS, and stained with 1 µg/mL PI for 10 min at room temperature in the dark. PI penetrates only cells with compromised membranes (dead cells). Analysis was performed on a CytoFLEX flow cytometer (Beckman Coulter, Brea, CA, USA). The proportion of PI-positive (non-viable) cells was calculated as a percentage of the total cell count. Measurements were performed in triplicate for each condition.

3. Results and Discussion

3.1. Optimization of Transition Zone Processing

The transition zone is a critical region in multi-material structures, governing the integrity of the bond between the Ti15Ta and Ti6Al4V alloys. Optimization of the processing parameters for this zone is aimed at minimizing porosity and forming a high-quality metallurgical bond.

Figure 4 presents optical micrographs of the transition zone cross-sections for the three investigated processing regimes. The interface between the Ti15Ta (upper part) and Ti6Al4V (lower part) alloys is characterized by the absence of macroscopic defects, such as delamination or large lack-of-fusion voids, in all regimes, indicating the compatibility of the selected processing parameters.

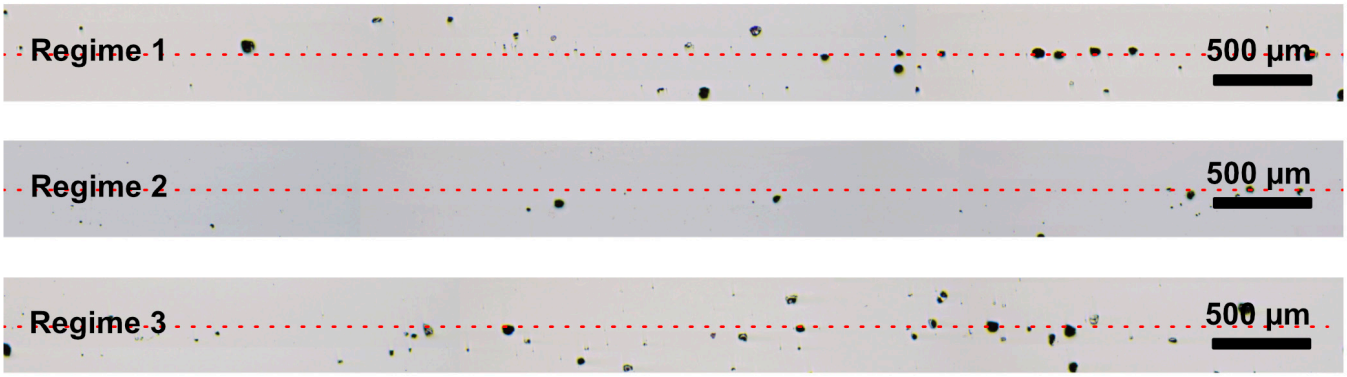


Figure 4. Cross-sectional optical micrographs of the transition zone under various processing conditions for Ti15Ta/Ti6Al4V multi-material.

Quantitative porosity evaluation of the transition zone by metallographic analysis (Table 3) revealed differences between the regimes. Baseline Regime 1 with a uniform energy density of 93 J/mm^3 provided a relative density of 98.2 ± 0.2%. Regime 3 with reduced scanning speed (energy density of 116 J/mm^3) showed a marginal improvement to 98.5 ± 0.2%. The best result was achieved with Regime 2 employing double scanning (energy density of 186 J/mm^3), where the relative density reached 99.49 ± 0.1%.

Table 3. Transition zone density values obtained by metallographic analysis.

	Regime 1	Regime 2	Regime 3
Metallographic Density (%)	98.2 ± 0.2	99.49 ± 0.1	98.5 ± 0.2

The improvement in density under double scanning may be attributed to several factors. First, remelting facilitates the healing of pores formed during the first laser pass [41]. Second, the additional thermal cycle promotes more complete degassing of the melt and removal of entrapped shielding gas. Third, the increased energy input compensates for potential non-uniformity in laser radiation absorption at the boundary between two powders with different optical properties.

Regime 3 with reduced scanning speed demonstrated a less pronounced improvement in density compared to double scanning, despite an increase in volumetric energy density to 116 J/mm^3. This result is explained by the difference in the mechanisms affecting porosity.

A reduction in scanning speed produces a deeper melt pool; however, excessive energy input increases the risk of keyhole formation, in which metal vapor pressure creates a vapor-gas cavity [42]. Upon its collapse, vapor and shielding gas become entrapped in the solidifying material, forming spherical pores. Thus, reducing the scanning speed produces competing effects: more complete powder melting on the one hand, but an elevated risk of keyhole porosity on the other.

3.2. Microstructure of As-Built and After Heat Treatment Samples

The microstructure of both alloys in the as-built L-PBF condition consists of metastable α′ martensite, the formation of which is driven by the high cooling rates characteristic of the laser fusion process. Heat treatment at 875 °C for 2 h results in the decomposition of α′ martensite and the formation of an equilibrium lamellar (α + β) structure. Figure 5 presents the XRD patterns of the Ti15Ta alloy in the as-built and heat-treated conditions, confirming the phase transformation: the as-built condition is characterized by peaks corresponding to the α′/α phase, while after heat treatment, additional β-phase peaks appear, indicating the formation of the equilibrium (α + β) microstructure. For the Ti6Al4V alloy, the α′→(α + β) decomposition under similar heat treatment conditions has been well documented in previous studies [43]. The following discussion focuses primarily on the morphology of the transition zone between Ti15Ta and Ti6Al4V.

Figure 6 presents SEM images of the transition zone between Ti15Ta and Ti6Al4V for the different printing regimes in the as-built condition.

A comparison of the processing regimes revealed significant differences in the transition zone morphology. In Regime 1 (Figure 6a), melt pool depths range from 60 to 110 μm. A characteristic feature is the non-uniform contrast distribution within the melt pools, indicating incomplete mixing of the melt under rapid solidification conditions.

Regime 2 with double scanning (Figure 6b) demonstrates the greatest melt pool depth among the investigated regimes, reaching 150–200 μm. The repeated laser exposure provides remelting of previously solidified material, which is morphologically manifested as two successive solidification fronts within a single melt pool. The most significant distinction of this regime is the formation of a pronounced homogeneous mixing layer with a thickness of 150–200 μm, characterized by uniform contrast in the BSE image.

Regime 3 with reduced scanning speed (Figure 6c) is characterized by melt pool depths of 110–180 μm due to the increased laser–material interaction time. However, despite the elevated energy input, regions with non-uniform contrast, similar to those in Regime 1, are present within the melt pools.

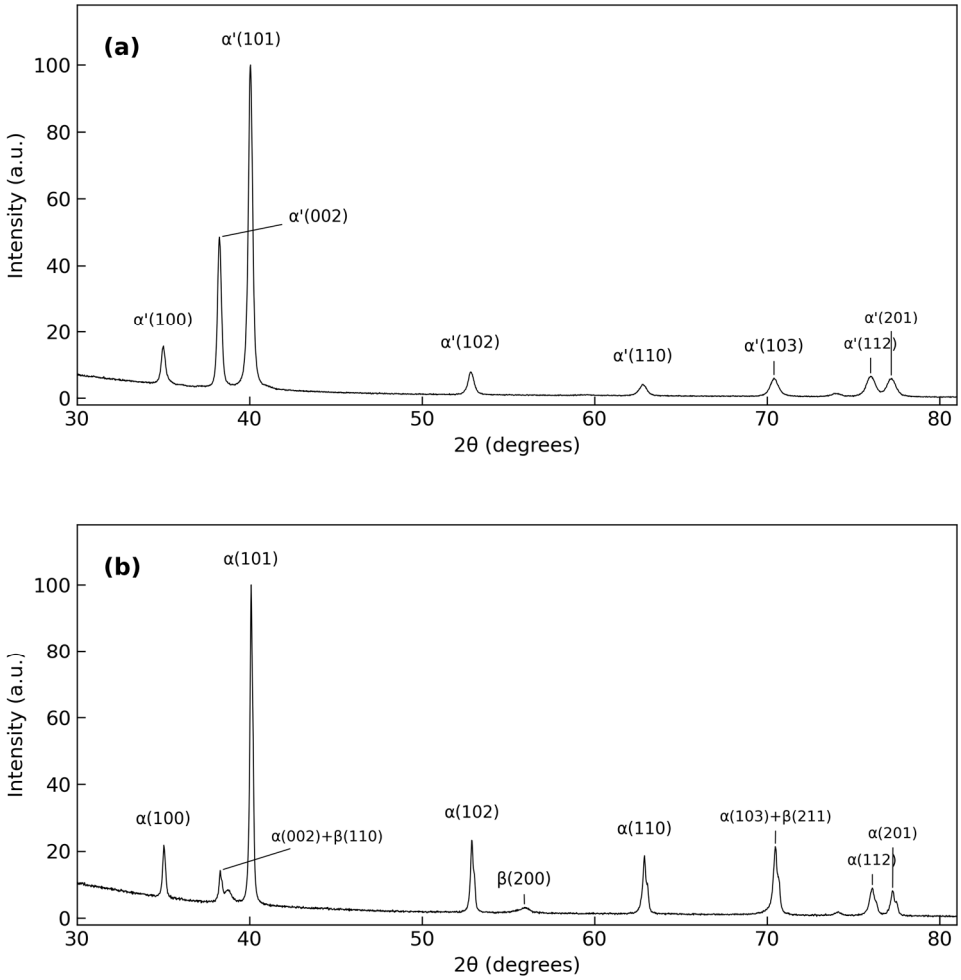


Figure 5. XRD patterns of the Ti15Ta alloy: (**a**) as-built condition; (**b**) after heat treatment (875 °C, 2 h).

It should be noted that visual non-uniformity of the transition zone morphology is observed across all regimes, manifested as considerable scatter in melt pool depth, variation in layer thickness, and alternation of melt pools oriented perpendicular and parallel to the cross-sectional plane. These features are attributed to the non-uniform deposition of Ti15Ta powder onto the solidified Ti6Al4V surface during the material changeover.

It should be noted that the nominal thickness of the transition zone is defined by the process design and corresponds to five layers with a cumulative thickness of 250 μm. However, direct quantitative measurement of the actual mixing layer thickness for comparison between regimes is complicated by the substantial spatial non-uniformity of the transition zone across the specimen cross-section. This non-uniformity arises from the inherent irregularity of powder deposition during the material changeover procedure: the first Ti15Ta layers deposited onto the solidified Ti6Al4V surface exhibit considerable variation in local layer thickness and powder packing density. As a result, the measurement uncertainty associated with the transition zone thickness substantially exceeds the expected differences between regimes, which are primarily determined by the variation in melt pool depth of the first deposited layer. For this reason, the melt pool depth and the presence or absence of a homogeneous mixing layer, rather than the overall transition zone thickness, are considered more representative quantitative metrics for comparing the effectiveness of the investigated processing regimes.

An additional factor that may contribute to the observed compositional inhomogeneity of the transition zone is the substantial difference in particle size distribution between the two powders: Ti15Ta (d50 = 35.2 μm) is significantly finer than Ti6Al4V (d50 = 67 μm).

This disparity may affect the transition zone through several mechanisms. The finer Ti15Ta particles possess a higher specific surface area, which increases laser radiation absorption and may result in altered melt pool dynamics compared to the steady-state conditions established for coarser Ti6Al4V powder. Furthermore, the difference in particle size influences the Marangoni-driven convective flows within the melt pool: when finer Ti15Ta particles are melted on the surface of solidified Ti6Al4V, the resulting gradients in surface tension and melt viscosity may differ from those in a single-material process, impeding complete compositional homogenization within the short solidification time inherent to L-PBF. The double scanning regime (Regime 2) effectively compensates for these effects by providing an additional thermal cycle that extends the time available for convective mixing and promotes the formation of a homogeneous mixing layer, as described above.

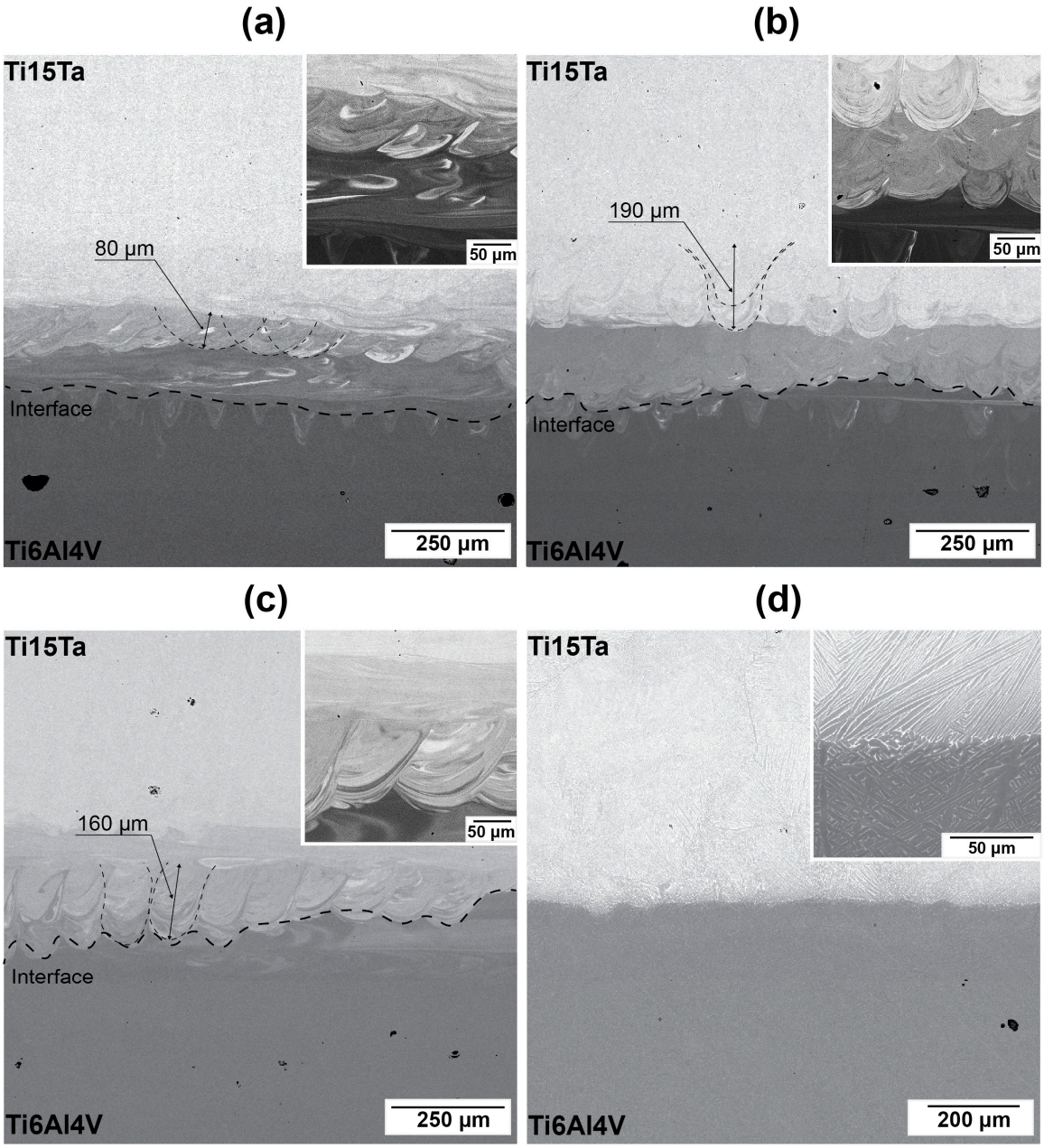


Figure 6. SEM micrographs of the transition zone microstructure: (**a**) processing regime 1; (**b**) processing regime 2; (**c**) processing regime 3; (**d**) after heat treatment. Dashed lines indicate melt pool boundaries.

Heat treatment leads to a substantial transformation of the transition zone morphology (Figure 6d). The wavy character of the interface, defined by the melt pool geometry, is completely eliminated as a result of diffusion processes, and the interface assumes the appearance of a straight line. The decomposition of metastable α′ martensite is accompanied by the formation of an equilibrium lamellar (α + β) microstructure with distinct morphologies in the two alloys: in Ti15Ta, α-lamellae exhibits a predominantly unidirectional orientation, whereas in Ti6Al4V, a more random structure with mutually intersecting lamellae is formed, characteristic of a basket-weave type microstructure.

For a detailed analysis of the alloying element distribution in the transition region, EDS mapping was performed for Ti, Ta, Al, and V (Figures 7 and 8).

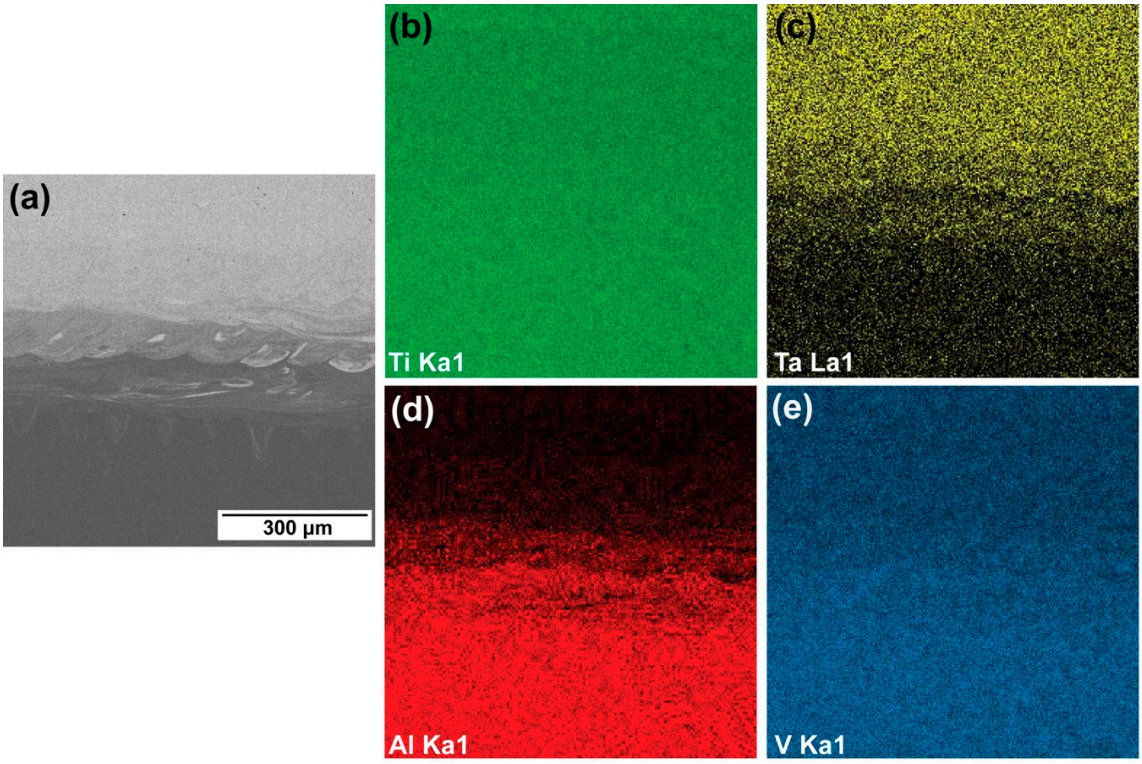


Figure 7. Elemental distribution across the transition zone under processing regime 1: (**a**) SEM micrograph of the analyzed region; elemental distribution maps: (**b**) titanium; (**c**) tantalum; (**d**) aluminum; (**e**) vanadium.

As-built condition (Figure 7). The EDS maps allow a direct interpretation of the contrast variations observed in the BSE images of the transition zone (Figure 6). In the as-built specimens, tantalum distribution maps reveal compositional inhomogeneity within the transition zone: the localized bright regions observed in Regime 1 (Figure 6a) correspond to Ta-enriched zones, confirming incomplete melt mixing under the rapid solidification conditions characteristic of the L-PBF process. The uniform contrast in Regime 2 (Figure 6b) is consistent with the homogeneous elemental distribution achieved by double scanning, whereas Regime 3, despite the elevated energy input, exhibits contrast inhomogeneity similar to Regime 1. The distribution of aluminum and vanadium exhibits a mirror pattern relative to tantalum, with a concentration maximum in the Ti6Al4V zone and a gradual decrease toward Ti15Ta.

To provide a quantitative assessment of the elemental distribution, point EDS analysis was performed across the transition zone at eight locations with a step of 150 μm (Figure 9). The resulting concentration profiles confirm the trends observed in the elemental maps.

In the Ti15Ta region (750–1050 μm from the Ti6Al4V side), the tantalum content remains stable at 15.99–16.40 at.%, while aluminum and vanadium are not detected. At a distance of 600 μm, the first traces of Al (0.39 at.%) and V (0.33 at.%) appear, indicating the onset of the transition zone, while tantalum decreases slightly to 15.09 at.%. Within the transition zone, a steep compositional gradient is observed: at 450 μm, the tantalum concentration drops to 9.48 at.% with a concurrent increase in aluminum to 2.27 at.% and vanadium to 1.73 at.%; at 300 μm, tantalum further decreases to 2.69 at.%, while aluminum and vanadium reach 4.77 and 3.55 at.%, respectively. In the Ti6Al4V region (0–150 μm), the composition stabilizes at 5.60–5.74 at.% Al and 3.95–4.10 at.% V, with no detectable tantalum. The measured profiles demonstrate that the compositional transition occurs over a distance of approximately 300–450 μm, which is consistent with the melt pool depth range reported for Regime 1 (60–110 μm) and the nominal five-layer transition design (250 μm).

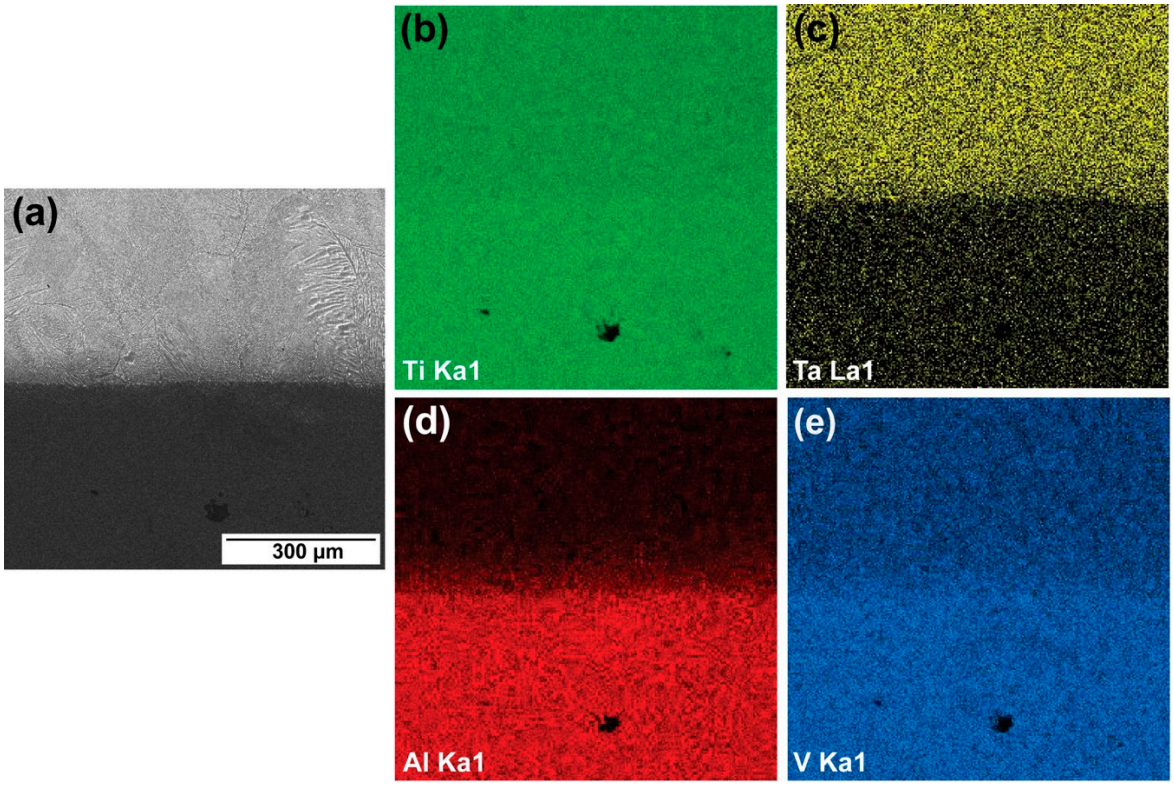


Figure 8. Elemental distribution across the transition zone after heat treatment: (**a**) SEM micrograph of the analyzed region; elemental distribution maps: (**b**) titanium; (**c**) tantalum; (**d**) aluminum; (**e**) vanadium.

Post-heat treatment condition (Figure 8). Annealing at 875 °C for 2 h leads to a transformation of the transition zone morphology. The wavy character of the interface is eliminated, and the boundary assumes the appearance of a sharp, well-defined line. This change is attributed to the occurrence of mutual elemental diffusion at elevated temperature. The elemental distribution maps demonstrate the formation of a smooth concentration gradient in the direction perpendicular to the interface. The smoothing of compositional discontinuities indicates the effective progression of diffusion processes under the selected heat treatment parameters.

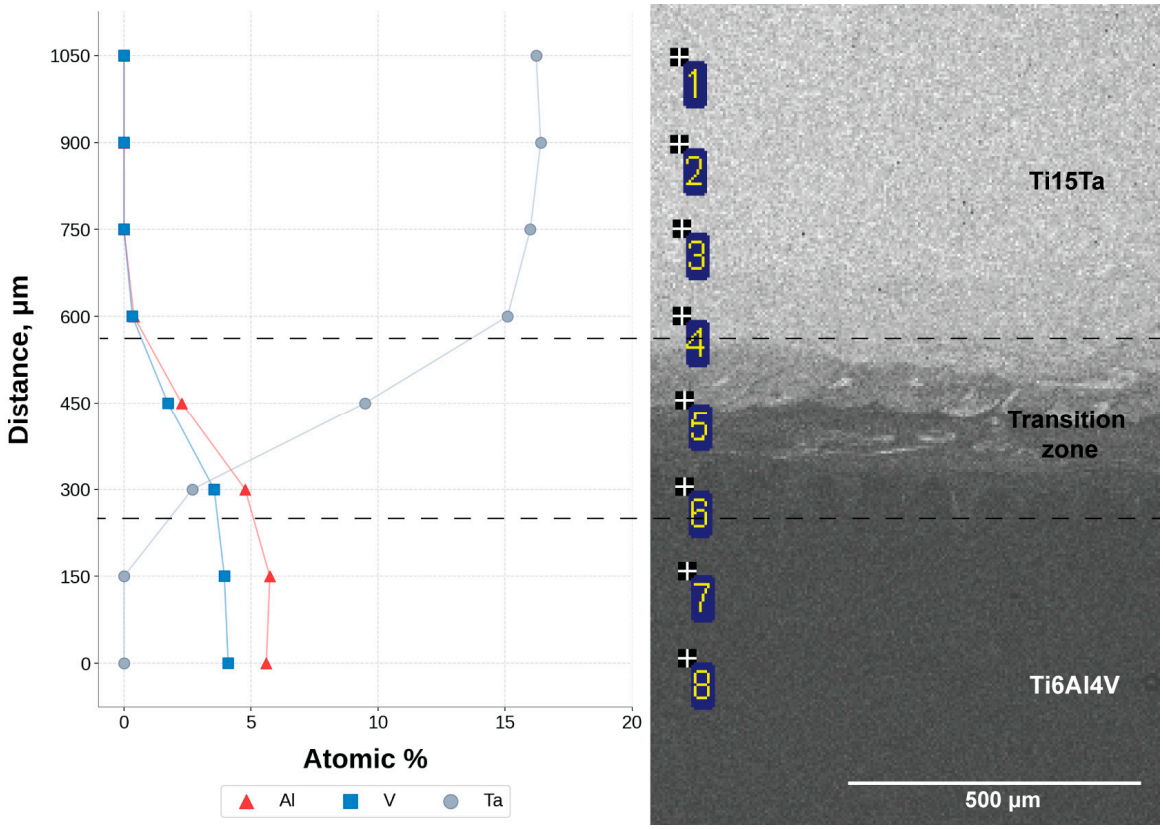


Figure 9. Quantitative elemental distribution (at.%) of Al, V, and Ta across the Ti15Ta/Ti6Al4V transition zone (Regime 1, as-built) obtained by point EDS analysis with a step of 150 µm, and corresponding SEM micrograph indicating measurement locations. Dashed lines denote the approximate boundaries of the transition zone.

3.3. Mechanical Properties

3.3.1. Tensile Properties

The mechanical properties of the multi-material Ti15Ta/Ti6Al4V specimens were evaluated by uniaxial tensile testing. Photographs of the fractured specimens (Figure 10) show that failure in all cases occurred in the Ti15Ta alloy region, which possesses lower strength compared to Ti6Al4V, indicating sufficient strength of the transition zone and a high-quality metallurgical bond between the two alloys.

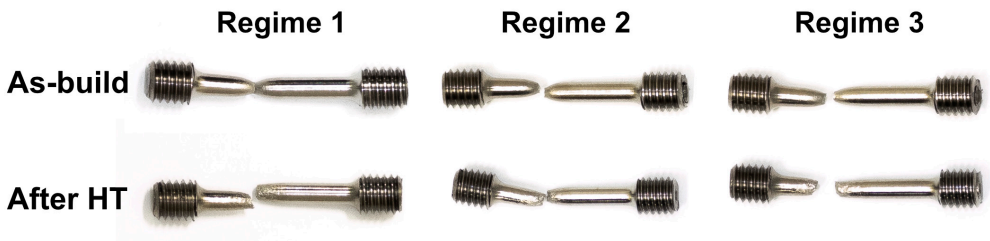


Figure 10. Photographs of specimens after tensile mechanical testing.

The stress–strain curves (Figure 11) demonstrate behavior characteristic of ductile metals, with a distinct elastic deformation region, a transition to plastic flow, and subsequent strain hardening up to failure. The test results for all processing regimes before and after heat treatment are presented in Table 4. It should be noted that the mechanical properties of Ti6Al4V reported in [38] correspond to the as-built condition without heat treatment,

where the presence of brittle α′ martensite results in high strength but limited ductility compared to typical values reported in the literature for heat-treated L-PBF Ti6Al4V.

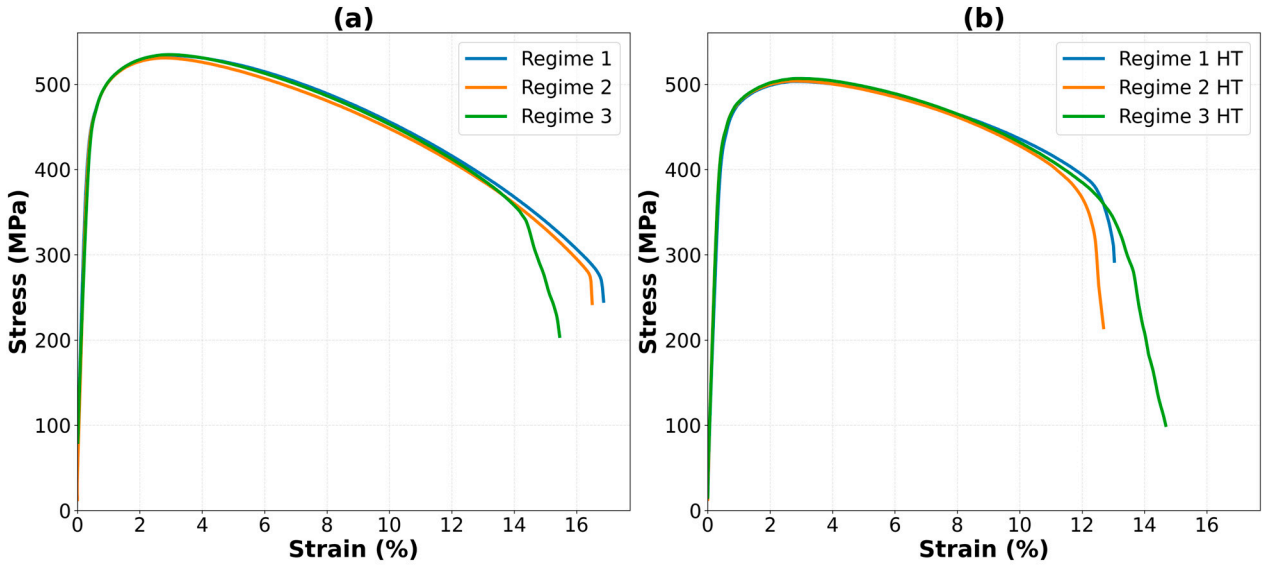


Figure 11. Tensile stress–strain curves for three processing conditions: (**a**) as-built; (**b**) after heat treatment.

Table 4. Summary of tensile properties for different processing regimes.

Regime/Alloy	Elastic Modulus (GPa)	Yield Strength (MPa)	Tensile Strength (MPa)	Elongation (%)	Reduction in Area (%)	References
Regime 1	125 ± 2	466 ± 7	538 ± 6	16.20 ± 0.73	72.36 ± 1.61	Current study
Regime 2	115 ± 11	467 ± 4	534 ± 4	16.37 ± 0.04	71.32 ± 0.86	Current study
Regime 3	103 ± 13	470 ± 18	535 ± 5	15.69 ± 0.42	68.74 ± 7.92	Current study
Regime 1 HT	94 ± 12	448 ± 14	503 ± 5	12.77 ± 0.24	38.42 ± 17.45	Current study
Regime 2 HT	110 ± 11	445 ± 11	504 ± 8	13.53 ± 0.17	49.05 ± 7.51	Current study
Regime 3 HT	111 ± 12	446 ± 12	507 ± 4	14.62 ± 0.74	61.92 ± 9.09	Current study
Ti15Ta	89 ± 3	468 ± 12	543 ± 13	21.1 ± 2.0	-	[37]
Ti6Al4V	-	1200	1280	2.4	-	[38]

A comparative analysis of the three transition zone processing regimes revealed no statistically significant differences in the mechanical properties of the as-built specimens. The high values of reduction in area (68.7–72.4%) indicate a ductile fracture mode with pronounced strain localization in the neck. The absence of substantial differences between the regimes suggests that the baseline regime with an energy density of 93 J/mm^3 is sufficient to form a high-quality bond, allowing the use of unified processing parameters for the entire component.

The elastic modulus of the multi-material specimens varied within the range of 103–125 GPa. The measured values reflect the composite nature of the specimen and fall between the elastic moduli of Ti6Al4V (~120 GPa) and Ti15Ta (89 GPa). It should be emphasized that the present bi-layer design does not demonstrate reduced stiffness compared to monolithic Ti6Al4V, and the elastic modulus remains substantially higher than that of human cortical bone (10–30 GPa) [44]. Accordingly, this work serves as a proof of concept for achieving high-quality metallurgical bonding between Ti15Ta and Ti6Al4V, rather than a final stiffness-optimized implant. Achieving the targeted reduction in elastic modulus in the bone contact zone will require further optimization of the implant architecture, including increasing

the volume fraction of Ti15Ta, incorporating porous structures, or implementing a fully functionally graded transition.

Given the limited sample size (n = 3 per regime), descriptive statistics (mean ± standard deviation) were used to characterize the mechanical properties. The overlapping standard deviation ranges between the three regimes suggest that the observed differences are not statistically significant, which is consistent with the conclusion that all regimes provide comparable bond quality. Regarding the large standard deviations of the elastic modulus (±11–13 GPa), it should be emphasized that uniaxial tensile testing is not the most accurate method for elastic modulus determination, as the measurement is highly sensitive to extensometer alignment, grip effects, and specimen geometry. These sources of uncertainty are further amplified in multi-material specimens of small dimensions, where variations in the relative contributions of Ti15Ta and Ti6Al4V to the overall deformation introduce additional scatter. More precise determination of the elastic modulus would require dedicated techniques such as nanoindentation or ultrasonic methods, which is beyond the scope of the present study.

Regime 2, which achieved the highest transition zone density (99.49%), did not demonstrate improved strength characteristics compared to Regimes 1 and 3. This indicates that the density level attained in all regimes is sufficiently high and does not constitute a limiting factor. Specimen failure occurred in the Ti15Ta region, away from the transition zone, confirming that the mechanical properties are governed by the characteristics of the weaker component rather than by the quality of the transition zone.

Heat treatment resulted in a decrease in strength characteristics and a reduction in elongation. As described in Section 3.2, annealing leads to the decomposition of metastable α' martensite and the formation of an equilibrium lamellar (α + β) microstructure. The resulting coarsening of α-lamellae reduces the density of interphase boundaries that impede dislocation motion, leading to a decrease in yield strength in accordance with the Hall–Petch relationship [45]. An additional contributing factor is the relaxation of residual stresses, a significant portion of which is relieved at temperatures above 500–600 °C [46].

The decrease in elongation after heat treatment may be associated with several factors. The formation of large α-lamella colonies promotes the localization of plastic deformation at colony boundaries [47]. Furthermore, the transition from a martensitic structure to a lamellar (α + β) structure alters the balance of deformation mechanisms: the contribution of twinning decreases while the role of dislocation slip increases [48].

It should also be noted that the measured elongation values are influenced by the composite nature of the gauge section. Since the ultimate tensile strength of the multi-material specimens (534–543 MPa) is well below the yield strength of Ti6Al4V (~1200 MPa), the Ti6Al4V portion of the gauge length remains in the elastic regime throughout the entire test and does not undergo plastic deformation. Consequently, plastic strain is confined to approximately one half of the gauge length occupied by Ti15Ta, while the other half contributes only elastic strain. The total elongation measured over the full gauge length (15 mm) is therefore lower than the intrinsic elongation of monolithic Ti15Ta (21.1 ± 2.0% [37]). This geometric effect is inherent to multi-material tensile specimens and should be taken into account when comparing the ductility of such specimens with that of single-material counterparts.

The obtained strength values of the multi-material specimens (503–543 MPa) are consistent with the strength of Ti15Ta, as expected, since fracture occurs precisely in this region. The elongation of the multi-material specimens (12.8–16.4%) exceeds the minimum requirements of the ASTM F3001-14 standard [49] for additively manufactured Ti6Al4V (≥10%), confirming the suitability of the developed materials for orthopedic applications.

3.3.2. Microhardness

The microhardness distribution across the Ti15Ta/Ti6Al4V transition zone was investigated by the Vickers method ($HV_{0.3}$). The measurement results are presented in Table 5 and in the microhardness profile plot (Figure 12).

Table 5. Microhardness measurement results through the transition zone.

Microhardness ($HV_{0.3}$)	Regime 1	Regime 2	Regime 3	Regime 1 HT
1	191 ± 7	185 ± 3	200 ± 11	174 ± 4
2	209 ± 5	172 ± 6	215 ± 6	176 ± 3
3	221 ± 3	232 ± 8	222 ± 3	180 ± 1
4	175 ± 9	291 ± 2	259 ± 8	195 ± 3
5	271 ± 1	304 ± 7	292 ± 2	202 ± 7
6	337 ± 6	360 ± 6	329 ± 3	235 ± 3
7	380 ± 6	343 ± 9	406 ± 6	320 ± 1
8	387 ± 10	367 ± 4	389 ± 10	314 ± 5
9	381 ± 5	367 ± 8	395 ± 3	332 ± 7
10	372 ± 7	370 ± 10	386 ± 7	320 ± 8

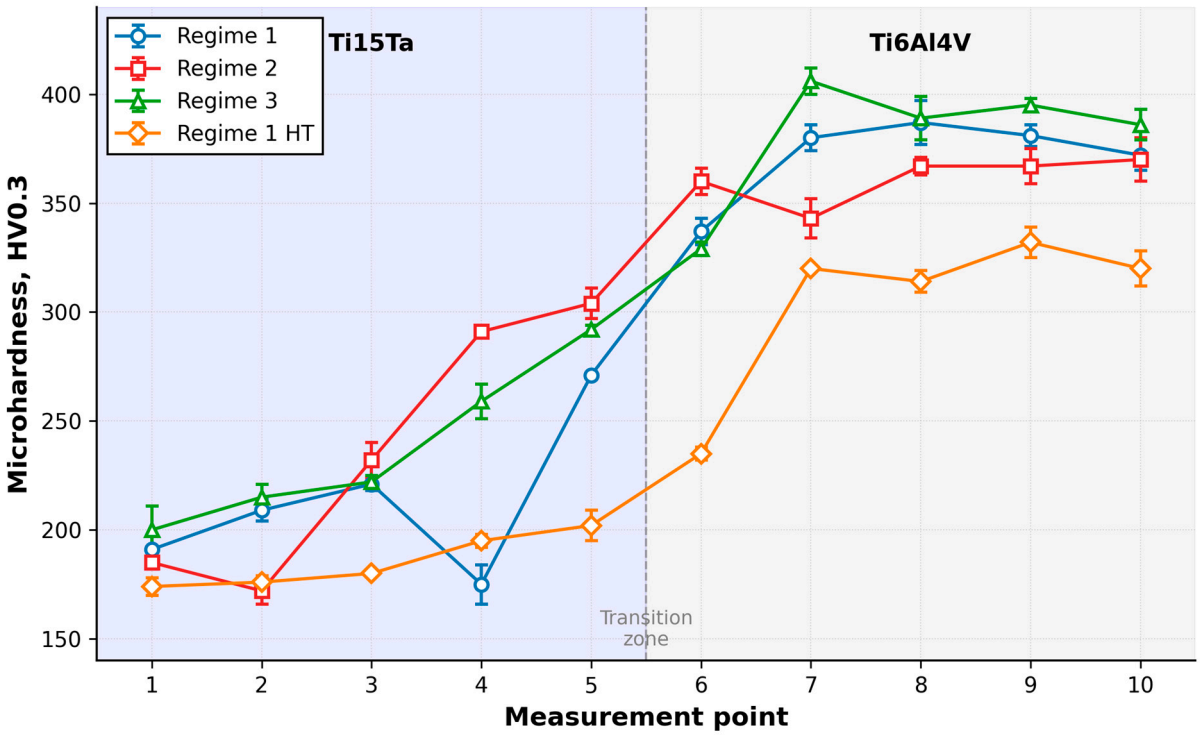


Figure 12. Microhardness distribution profiles across the Ti15Ta/Ti6Al4V transition zone.

The transition zone is characterized by a gradient change in hardness, reflecting the diffusional intermixing of the components and a gradual variation in phase composition.

A comparison of the different processing regimes shows that Regime 2 (double scanning) provides somewhat higher hardness values in the transition zone on the Ti6Al4V side (360 HV at position 6), which may be attributed to the more intense repeated thermal exposure and the formation of a finer microstructure.

Heat treatment leads to a substantial decrease in microhardness across all zones of the specimen, consistent with the microstructural changes discussed in Section 3.3.1.

The hardness profile after heat treatment becomes smoother, with a less abrupt transition between zones, indicating additional elemental diffusion across the interface during high-temperature annealing and homogenization of the transition region.

3.4. Biocompatibility Assessment

3.4.1. Cell Morphology by Scanning Electron Microscopy

Scanning electron microscopy revealed adhesion of both cell types on the Ti15Ta and Ti6Al4V surfaces after 120 h of culture (Figure 13). Both materials supported cell attachment; however, alterations in morphological characteristics were observed compared to standard culture conditions on tissue culture plastic.

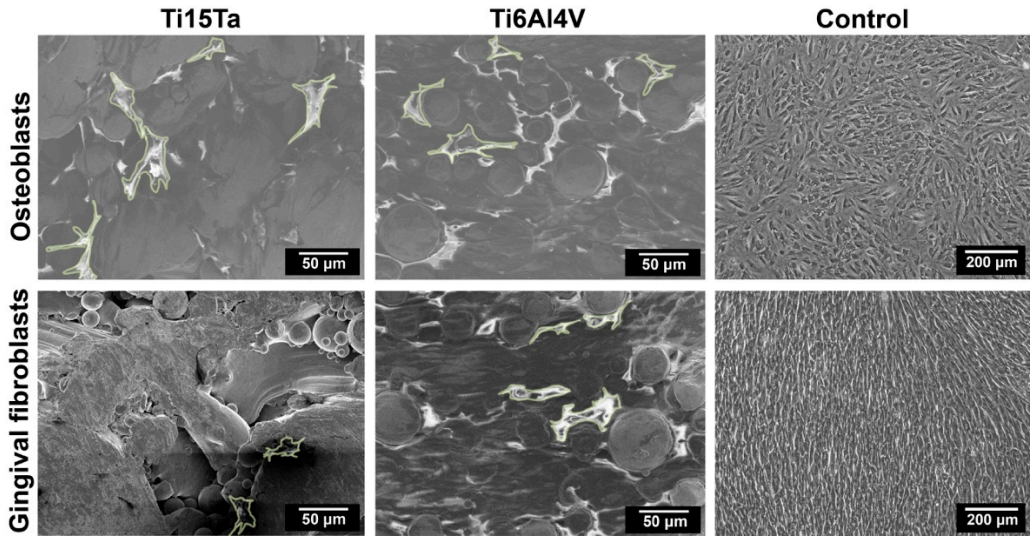


Figure 13. SEM images of osteoblasts and gingival fibroblasts on Ti15Ta and Ti6Al4V. Note: control images are shown at lower magnification to demonstrate overall cell coverage on tissue culture plastic. Green lines indicate cell contours.

Under standard conditions, osteoblasts are characterized by a polygonal morphology with evenly distributed processes, while gingival fibroblasts exhibit a spindle-shaped morphology with pronounced orientation of cytoplasmic processes. When cultured on titanium alloys, the morphological characteristics of the cells were altered: some osteoblasts acquired a more elongated shape with randomly directed processes, and gingival fibroblasts lost their characteristic oriented structure.

Comparative analysis showed that osteoblasts demonstrated more pronounced spreading and the formation of tight contacts on the Ti6Al4V surface, with the highest cell density observed on this material. For gingival fibroblasts, the differences between Ti15Ta and Ti6Al4V were less pronounced. The observed morphological changes reflect the specific cellular response to the surface chemical composition and microtopography resulting from mechanical processing of the titanium alloys [50], leading to adaptive reorganization of the cytoskeleton. It has previously been shown that cells on smooth titanium surfaces exhibit a flat, well-spread morphology with prominent stress fibers, whereas on rough surfaces cells acquire a more elongated shape with a less developed actin cytoskeleton; however, these morphological differences do not correlate with the functional activity of the cells [51].

It is important to note that morphological observations by SEM represent a qualitative assessment of localized surface areas, whereas objective quantitative evaluation of biocompatibility requires the application of standardized methods for assessing metabolic activity and cell viability, which provide statistically reliable information on the biological response to the material.

3.4.2. Evaluation of Metabolic Activity and Cytotoxicity

The MTT assay enabled quantitative evaluation of cell metabolic activity on Ti15Ta and Ti6Al4V surfaces over time at 48 and 120 h of culture (Figure 14) and (Table 6). The

results are expressed as percentages relative to the control group (cells on standard tissue culture plastic).

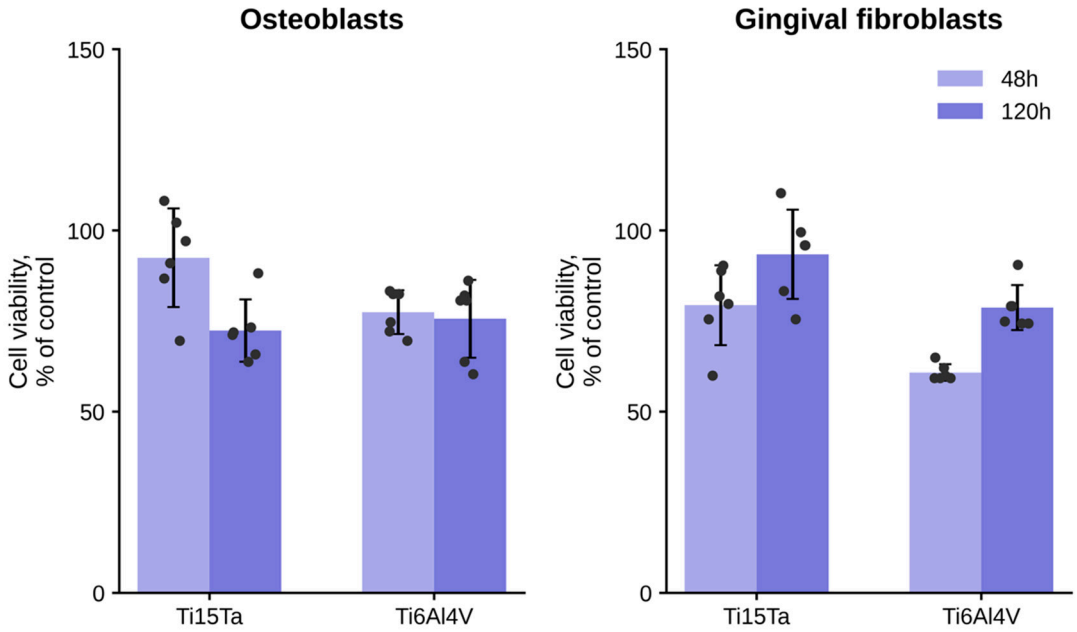


Figure 14. MTT assay results for osteoblasts and gingival fibroblasts at 48 h and 120 h.

Table 6. MTT assay results for osteoblasts and gingival fibroblasts at 48 h and 120 h.

	Ti15Ta 48 h	Ti15Ta 120 h	Ti6Al4V 48 h	Ti6Al4V 120 h
Osteoblasts	92.5 ± 13.6	72.4 ± 8.6	77.4 ± 6.0	75.6 ± 10.8
Gingival fibroblasts	79.4 ± 11	93.4 ± 12.3	60.8 ± 2.3	78.7 ± 6.2

Osteoblasts on both investigated materials maintained high viability throughout the entire observation period. On Ti15Ta, a slight decrease in the viability index was observed from 48 to 120 h. On Ti6Al4V, osteoblast viability remained virtually unchanged throughout the observation period, which is consistent with the SEM results, where more pronounced adhesion and preservation of typical morphological features were identified for this material.

Gingival fibroblasts demonstrated more pronounced dynamics in the measured parameters. At the initial measurement point (48 h), the cells showed reduced viability on both materials compared to the control, which may reflect initial adaptive stress upon interaction with the metallic surface. On both Ti15Ta and Ti6Al4V, viability was maintained at a comparable stable level without marked changes by 120 h, indicating successful adaptation of the cells to the surface of both materials.

According to the international standard ISO 10993-5, materials are considered non-cytotoxic if cell viability exceeds 70% of control values [52]. Analysis of the obtained values demonstrates that both investigated materials maintained cell viability above this threshold at the 120 h time point across all cell type–material combinations. At 48 h, gingival fibroblasts on Ti6Al4V exhibited a viability of 60.8 ± 2.3%, which is below the 70% threshold; however, this value increased to 78.7 ± 6.2% by 120 h. The transient reduction in metabolic activity at the early time point may be attributed to several factors. First, the release of aluminum and vanadium ions from the Ti6Al4V surface during the initial hours of contact with the culture medium may exert cytotoxic effects on fibroblasts, as demonstrated in several studies [4,5]. Second, the surface roughness and microtopography

resulting from mechanical grinding may influence the initial cell adhesion and subsequent proliferation [50,51]. The recovery of viability by 120 h suggests that the initial effect is transient and does not lead to sustained cytotoxicity, which is consistent with the formation of a stable TiO_2 oxide film on the alloy surface that limits further ion release [53]. It should be noted that surface roughness (Ra) measurements and quantitative ion release analysis were not performed in the present study, which precludes establishing a direct correlation between surface characteristics and biological response. A systematic investigation of the effects of surface roughness and ion release kinetics on the cellular response is warranted and will be addressed in future studies. For all other cell type–material combinations, viability remained above 70% at both time points. No statistically significant differences in cell viability were observed between Ti15Ta and Ti6Al4V for either cell type at both time points ($p > 0.05$, Mann–Whitney U test).

3.4.3. Quantitative Viability Assessment by Flow Cytometry

Flow cytometry analysis with propidium iodide staining provided precise quantitative assessment of cell viability after 120 h of culture on titanium surfaces (Table 7).

Table 7. Percentage of live and dead cells.

Cell Type	Matrix Type	Fraction of Live Cells	Fraction of Dead Cells
Osteoblasts	Control	94.43%	4.87%
	Ti15Ta	88.62%	5.07%
	Ti6Al4V	90.67%	7.04%
Gingival fibroblasts	Control	94.10%	5.67%
	Ti15Ta	97.11%	1.85%
	Ti6Al4V	95.25%	4.47%

It should be noted that the sum of the live and dead cell fractions does not reach 100%. In single-stain PI flow cytometry, events are classified by fluorescence intensity as either PI-negative (live) or PI-positive (dead). However, a fraction of detected events—including cell fragments and debris—exhibits intermediate fluorescence and falls outside both analytical gates, accounting for the remainder.

Osteoblasts maintained high viability on both materials: 88.62% viable cells on Ti15Ta and 90.67% on Ti6Al4V compared to 94.43% in the control group (Table 7). The proportion of dead cells remained low at 5.07% and 7.04%, respectively. Gingival fibroblasts demonstrated comparable viability values: 97.11% on Ti15Ta and 95.25% on Ti6Al4V compared to 94.10% in the control, with minimal dead cell fractions of 1.85% and 4.47%, respectively.

The somewhat higher survival rate of gingival fibroblasts on Ti15Ta compared to the control (97.11% versus 94.10%) may be attributed to the high bioinertness of tantalum. The Ta_2O_5 oxide film that forms on the alloy surface is characterized by high chemical stability and promotes the adsorption of extracellular matrix proteins, which may create more favorable conditions for fibroblast adhesion and survival [54].

The differences in the fractions of viable cells between Ti15Ta and Ti6Al4V were not statistically significant for either osteoblasts or gingival fibroblasts ($p > 0.05$, Mann–Whitney U test).

The obtained viability values for osteoblasts and fibroblasts are consistent with literature data for titanium alloys. In a comparative study of titanium and its alloys, fibroblast viability above 90% was reported for Ti6Al4V at various extract concentrations [55]. Various studies of titanium alloys have shown that the viability of osteoblasts and fibroblasts on titanium alloys with biocompatible alloying elements (Nb, Ta, Zr) consistently exceeds 85–90% [56].

4. Conclusions

In the present work, the fabrication of multi-material Ti15Ta/Ti6Al4V structures by laser powder bed fusion (L-PBF) was realized for the first time, and a comprehensive investigation of the effects of processing parameters on the transition zone quality, microstructure, mechanical properties, and biocompatibility of the obtained materials was conducted. The main findings of this study are as follows:

1. Optimization of transition zone parameters. It was established that the double scanning regime (energy density of 186 J/mm^3) provides the maximum relative density of the transition zone of 99.49 $\pm$ 0.1%, which is attributed to pore healing during remelting and more effective degassing of the melt.
2. Microstructural features. In the as-built condition, the transition zone is characterized by a wavy interface, the morphology of which is defined by the melt pool geometry. EDS mapping revealed incomplete compositional homogenization with localized Ta-enriched regions. Heat treatment at 875 °C for 2 h leads to the formation of a smooth interface with a gradual elemental concentration gradient, indicating the effective progression of diffusion processes.
3. Mechanical properties. Tensile failure of the multi-material specimens occurred in the Ti15Ta region, away from the transition zone, confirming the sufficient strength of the metallurgical bond. The mechanical characteristics of the multi-material specimens (ultimate tensile strength of 534–543 MPa, elongation of 15.7–16.4%) are governed by the properties of the Ti15Ta alloy as the weaker component of the system. Annealing leads to a reduction in strength characteristics (ultimate tensile strength to 503–507 MPa) and microhardness due to the decomposition of metastable α' martensite with the formation of an equilibrium lamellar (α + β) structure. At the same time, the hardness profile becomes smoother, indicating homogenization of the transition region.
4. Biocompatibility. Both alloys demonstrate high biocompatibility: the viability of osteoblasts and gingival fibroblasts on both alloys exceeded the 70% non-cytotoxicity threshold (ISO 10993-5), with flow cytometry confirming cell viability in the range of 88–97%.
5. Future studies should focus on the evaluation of cell response directly on the multi-material transition zone, fatigue testing of multi-material specimens, systematic investigation of surface roughness and ion release kinetics to establish correlations with biological response, and the fabrication of patient-specific implant prototypes with functionally graded architecture.

Thus, the results of this study confirm the technological feasibility of fabricating multi-material Ti15Ta/Ti6Al4V structures by L-PBF and demonstrate the formation of high-quality metallurgical bonding between the two alloys. The present work serves as a proof of concept for metallurgical joining and establishes a scientific foundation for the further development of next-generation functionally graded orthopedic implants capable of combining high mechanical strength of the internal framework with reduced stiffness of the outer layer to minimize the stress-shielding effect.

Author Contributions: Conceptualization, I.P.; data curation, A.P.; Methodology, I.P.; investigation, V.S., A.Z., V.N. and S.C.; visualization, V.N. and A.Z.; writing—original draft, A.Z., V.N. and S.C.; funding acquisition, A.P.; project administration, A.P.; supervision, I.P.; writing—review and editing, I.P. and A.P. All authors have read and agreed to the published version of the manuscript.

Funding: This research was supported by a grant from the Russian Science Foundation No. 25-79-00097.

Institutional Review Board Statement: This study was approved by the local Ethical Committee of Vreden National Medical Research Center of Traumatology and Orthopedics (Saint Petersburg,

Russia). Primary human osteoblasts were isolated from femur bone explants at the Institute of Cytology of the Russian Academy of Sciences (St. Petersburg, Russia) in accordance with the approved institutional protocols. Written informed consent was obtained from all donors. Human gingival fibroblasts were purchased from the Pokrovsky Stem Cell Bank (St. Petersburg, Russia), a commercial source. The study was conducted in accordance with the Declaration of Helsinki.

Informed Consent Statement: Informed consent was obtained from all subjects involved in the study.

Data Availability Statement: The data presented in this study are available on request from the corresponding author due to intellectual property restrictions related to ongoing research projects.

Acknowledgments: The authors acknowledge the Institute of Cytology of the Russian Academy of Sciences (St. Petersburg, Russia) for conducting the in vitro biocompatibility studies. The authors are grateful to A. B. Malashicheva, D. A. Serdyukova, V. A. Nyrov, and A. Babakovskaya for performing cell culture experiments, MTT assays, flow cytometry analysis, and SEM examination of cell–material interactions.

Conflicts of Interest: The authors declare no conflicts of interest.

References

1. Kacsó, A.-B.; Peter, I. A Review of Past Research and Some Future Perspectives Regarding Titanium Alloys in Biomedical Applications. *J. Funct. Biomater.* **2025**, *16*, 144. [CrossRef]
2. Tipan, N.; Pandey, A.; Mishra, P. Material Synthesis and Design Optimization of Biomaterials for Biomedical Implant Applications. *BioImpacts* **2024**, *15*, 30010. [CrossRef]
3. Cao, S.; Zou, Y.; Lim, C.V.S.; Wu, X. Review of Laser Powder Bed Fusion (LPBF) Fabricated Ti-6Al-4V: Process, Post-Process Treatment, Microstructure, and Property. *Light Adv. Manuf.* **2021**, *2*, 1. [CrossRef]
4. Costa, B.C.; Tokuhara, C.K.; Rocha, L.A.; Oliveira, R.C.; Lisboa-Filho, P.N.; Costa Pessoa, J. Vanadium Ionic Species from Degradation of Ti-6Al-4V Metallic Implants: In Vitro Cytotoxicity and Speciation Evaluation. *Mater. Sci. Eng. C* **2019**, *96*, 730–739. [CrossRef] [PubMed]
5. Toledano-Serrabona, J.; Gil, F.J.; Camps-Font, O.; Valmaseda-Castellón, E.; Gay-Escoda, C.; Sánchez-Garcés, M.Á. Physicochemical and Biological Characterization of Ti6Al4V Particles Obtained by Implantoplasty: An In Vitro Study. Part I. *Materials* **2021**, *14*, 6507. [CrossRef] [PubMed]
6. Khadija, G.; Saleem, A.; Akhtar, Z.; Naqvi, Z.; Gull, M.; Masood, M.; Mukhtar, S.; Batool, M.; Saleem, N.; Rasheed, T.; et al. Short Term Exposure to Titanium, Aluminum and Vanadium (Ti 6Al 4V) Alloy Powder Drastically Affects Behavior and Antioxidant Metabolites in Vital Organs of Male Albino Mice. *Toxicol. Rep.* **2018**, *5*, 765–770. [CrossRef]
7. Andrade del Olmo, J.; Alonso, J.M.; Ronco-Campaña, A.; Sáez-Martínez, V.; Pérez-González, R.; Rothnie, A.J.; Tighe, B.J.; Vilas-Vilela, J.L.; Pérez-Álvarez, L. Effectiveness of Physicochemical Techniques on the Activation of Ti6Al4V Surface with Improved Biocompatibility and Antibacterial Properties. *Surf. Coat. Technol.* **2022**, *447*, 128821. [CrossRef]
8. Kanapaakala, G.; Subramani, V. A Review on β-Ti Alloys for Biomedical Applications: The Influence of Alloy Composition and Thermomechanical Processing on Mechanical Properties, Phase Composition, and Microstructure. *Proc. Inst. Mech. Eng. Part L J. Mater. Des. Appl.* **2023**, *237*, 1251–1294. [CrossRef]
9. Safavi, S.; Yu, Y.; Robinson, D.L.; Gray, H.A.; Ackland, D.C.; Lee, P.V.S. Additively Manufactured Controlled Porous Orthopedic Joint Replacement Designs to Reduce Bone Stress Shielding: A Systematic Review. *J. Orthop. Surg. Res.* **2023**, *18*, 42. [CrossRef] [PubMed]
10. Guo, C.; Ding, T.; Cheng, Y.; Zheng, J.; Fang, X.; Feng, Z. The Rational Design, Biofunctionalization and Biological Properties of Orthopedic Porous Titanium Implants: A Review. *Front. Bioeng. Biotechnol.* **2025**, *13*, 1548675. [CrossRef]
11. Wang, X.; Wang, Y.; Xia, Z.; Zhou, Z.; Yang, W.; Yang, K. Preparation Methods, Microstructure and Properties of Ti-Ta Alloys: A Review. *Int. J. Adv. Manuf. Technol.* **2026**, *142*, 39–55. [CrossRef]
12. Polozov, I.; Nefyodova, V.; Zolotarev, A.; Sokolova, V.; Gracheva, A.; Popovich, A. Development of Low-Modulus Ti-Ta Alloys by in-Situ Synthesis during Selective Laser Melting for Implant Applications. *J. Alloys Compd.* **2025**, *1021*, 179682. [CrossRef]
13. Zhou, Y.-L.; Niinomi, M. Microstructures and Mechanical Properties of Ti–50mass% Ta Alloy for Biomedical Applications. *J. Alloys Compd.* **2008**, *466*, 535–542. [CrossRef]
14. Liu, Q.; Zhang, Y.; Chen, W.; He, P.; Tian, Y.; Liu, Y.; Dou, Y.; Bian, H.; Yang, J.; Yang, Q.; et al. Bioactive and Fatigue-Resistant Ti–Ta Alloy by Additive Manufacturing for Orthopedic Applications. *Smart Mater. Manuf.* **2025**, *3*, 100086. [CrossRef]
15. Yan, L.; Yuan, Y.; Ouyang, L.; Li, H.; Mirzasadeghi, A.; Li, L. Improved Mechanical Properties of the New Ti-15Ta-XZr Alloys Fabricated by Selective Laser Melting for Biomedical Application. *J. Alloys Compd.* **2016**, *688*, 156–162. [CrossRef]

16. Li, Y.; Feng, Z.; Hao, L.; Huang, L.; Xin, C.; Wang, Y.; Bilotti, E.; Essa, K.; Zhang, H.; Li, Z.; et al. A Review on Functionally Graded Materials and Structures via Additive Manufacturing: From Multi-Scale Design to Versatile Functional Properties. *Adv. Mater. Technol.* **2020**, *5*, 1900981. [CrossRef]
17. Najibi, A.; Mokhtari, T. Functionally Graded Materials for Knee and Hip Arthroplasty; an Update on Design, Optimization, and Manufacturing. *Compos. Struct.* **2023**, *322*, 117350. [CrossRef]
18. Rouf, S.; Malik, A.; Raina, A.; Irfan Ul Haq, M.; Naveed, N.; Zolfagharian, A.; Bodaghi, M. Functionally Graded Additive Manufacturing for Orthopedic Applications. *J. Orthop.* **2022**, *33*, 70–80. [CrossRef]
19. Zhu, C.; Gemeda, H.B.; Duoss, E.B.; Spadaccini, C.M. Toward Multiscale, Multimaterial 3D Printing. *Adv. Mater.* **2024**, *36*, e2314204. [CrossRef] [PubMed]
20. Mehrpouya, M.; Tuma, D.; Vaneker, T.; Afrasiabi, M.; Bambach, M.; Gibson, I. Multimaterial Powder Bed Fusion Techniques. *Rapid Prototyp. J.* **2022**, *28*, 1–19. [CrossRef]
21. Verma, A.; Kapil, A.; Klobčar, D.; Sharma, A. A Review on Multiplicity in Multi-Material Additive Manufacturing: Process, Capability, Scale, and Structure. *Materials* **2023**, *16*, 5246. [CrossRef]
22. Sefene, E.M. State-of-the-Art of Selective Laser Melting Process: A Comprehensive Review. *J. Manuf. Syst.* **2022**, *63*, 250–274. [CrossRef]
23. Zhang, L.-C.; Attar, H.; Calin, M.; Eckert, J. Review on Manufacture by Selective Laser Melting and Properties of Titanium Based Materials for Biomedical Applications. *Mater. Technol.* **2016**, *31*, 66–76. [CrossRef]
24. Tshephe, T.S.; Akinwamide, S.O.; Olevsky, E.; Olubambi, P.A. Additive Manufacturing of Titanium-Based Alloys- A Review of Methods, Properties, Challenges, and Prospects. *Heliyon* **2022**, *8*, e09041. [CrossRef]
25. Su, J.; Jiang, F.; Teng, J.; Chen, L.; Requena, G.; Yan, M.; Zhang, L.; Wang, Y.M.; Okulov, I.V.; Zhu, H.; et al. Laser Additive Manufacturing of Titanium Alloys: Process, Materials and Post-processing. *Rare Met.* **2024**, *43*, 6288–6328. [CrossRef]
26. Zhang, Y.; Wu, S.; Guo, Z.; Peng, G.; Wang, L.; Yan, W. Defects Caused by Powder Spattering and Entrainment in Laser Powder Bed Fusion Process: High-Fidelity Modeling of Gas, Melt Pool and Powder Dynamics. *Acta Mater.* **2025**, *288*, 120816. [CrossRef]
27. Cacace, S.; Semeraro, Q. On the Lack of Fusion Porosity in L-PBF Processes. *Procedia CIRP* **2022**, *112*, 352–357. [CrossRef]
28. Mojumder, S.; Gan, Z.; Li, Y.; Al Amin, A.; Liu, W.K. Linking Process Parameters with Lack-of-Fusion Porosity for Laser Powder Bed Fusion Metal Additive Manufacturing. *Addit. Manuf.* **2023**, *68*, 103500. [CrossRef]
29. Kim, F.H.; Moylan, S.P. *Literature Review of Metal Additive Manufacturing Defects*; National Institute of Standards and Technology: Gaithersburg, MD, USA, 2018.
30. Fan, H.; Wang, C.; Tian, Y.; Zhou, K.; Yang, S. Laser Powder Bed Fusion (L-PBF) of Ti–6Al–4V/Ti–6Al–2Sn–4Zr–2Mo and Ti–6Al–4V/γ-TiAl Bimetals: Processability, Interface and Mechanical Properties. *Mater. Sci. Eng. A* **2023**, *871*, 144907. [CrossRef]
31. Zhao, D.; Han, C.; Li, Y.; Li, J.; Zhou, K.; Wei, Q.; Liu, J.; Shi, Y. Improvement on Mechanical Properties and Corrosion Resistance of Titanium-Tantalum Alloys in-Situ Fabricated via Selective Laser Melting. *J. Alloys Compd.* **2019**, *804*, 288–298. [CrossRef]
32. Wu, Z.; Wilson-Heid, A.E.; Griffiths, R.J.; Elton, E.S. A Review on Experimentally Observed Mechanical and Microstructural Characteristics of Interfaces in Multi-Material Laser Powder Bed Fusion. *Front. Mech. Eng.* **2023**, *9*, 1087021. [CrossRef]
33. Borisov, E.; Polozov, I.; Starikov, K.; Popovich, A.; Sufiiarov, V. Structure and Properties of Ti/Ti64 Graded Material Manufactured by Laser Powder Bed Fusion. *Materials* **2021**, *14*, 6140. [CrossRef]
34. Bartolomeu, F.; Costa, M.M.; Alves, N.; Miranda, G.; Silva, F.S. Additive Manufacturing of NiTi-Ti6Al4V Multi-Material Cellular Structures Targeting Orthopedic Implants. *Opt. Lasers Eng.* **2020**, *134*, 106208. [CrossRef]
35. Zhang, J.; Wang, X.; Gao, J.; Zhang, L.; Song, B.; Zhang, L.; Yao, Y.; Lu, J.; Shi, Y. Additive Manufacturing of Ti–6Al–4V/Al–Cu–Mg Multi-Material Structures with a Cu Interlayer. *Int. J. Mech. Sci.* **2023**, *256*, 108477. [CrossRef]
36. Walker, J.; Middendorf, J.R.; Lesko, C.C.C.; Gockel, J. Multi-Material Laser Powder Bed Fusion Additive Manufacturing in 3-Dimensions. *Manuf. Lett.* **2022**, *31*, 74–77. [CrossRef]
37. Polozov, I.; Nefyodov, V.; Zolotarev, A.; Sokolova, V.; Gracheva, A.; Popovich, A. Process-Structure–Property Relationships in Selective Laser Melting of Ti-15Ta Alloy for Biomedical Applications. *Int. J. Adv. Manuf. Technol.* **2025**, *139*, 3391–3406. [CrossRef]
38. Polozov, I.; Gracheva, A.; Popovich, A. Interface Characterization of Bimetallic Ti-6Al-4V/Ti2AlNb Structures Prepared by Selective Laser Melting. *Materials* **2022**, *15*, 8528. [CrossRef]
39. *ASTM E8/E8M*; Standard Test Methods for Tensile Testing of Metallic Materials. ASTM International: West Conshohocken, PA, USA, 2021.
40. Kostina, D.; Lobov, A.; Klausen, P.; Karelkin, V.; Tikhilov, R.; Bozhkova, S.; Sereda, A.; Ryumina, N.; Enukashvily, N.; Malashicheva, A. Isolation of Human Osteoblast Cells Capable for Mineralization and Synthetizing Bone-Related Proteins In Vitro from Adult Bone. *Cells* **2022**, *11*, 3356. [CrossRef]
41. Yasa, E.; Deckers, J.; Kruth, J. The Investigation of the Influence of Laser Re-melting on Density, Surface Quality and Microstructure of Selective Laser Melting Parts. *Rapid Prototyp. J.* **2011**, *17*, 312–327. [CrossRef]

42. King, W.E.; Barth, H.D.; Castillo, V.M.; Gallegos, G.F.; Gibbs, J.W.; Hahn, D.E.; Kamath, C.; Rubenchik, A.M. Observation of Keyhole-Mode Laser Melting in Laser Powder-Bed Fusion Additive Manufacturing. *J. Mater. Process. Technol.* **2014**, *214*, 2915–2925. [CrossRef]
43. He, J.; Li, D.; Jiang, W.; Ke, L.; Qin, G.; Ye, Y.; Qin, Q.; Qiu, D. The Martensitic Transformation and Mechanical Properties of Ti6Al4V Prepared via Selective Laser Melting. *Materials* **2019**, *12*, 321. [CrossRef]
44. Niinomi, M.; Nakai, M. Titanium-Based Biomaterials for Preventing Stress Shielding between Implant Devices and Bone. *Int. J. Biomater.* **2011**, *2011*, 836587. [CrossRef] [PubMed]
45. Hansen, N. Hall–Petch Relation and Boundary Strengthening. *Scr. Mater.* **2004**, *51*, 801–806. [CrossRef]
46. Ter Haar, G.; Becker, T. Selective Laser Melting Produced Ti-6Al-4V: Post-Process Heat Treatments to Achieve Superior Tensile Properties. *Materials* **2018**, *11*, 146. [CrossRef]
47. Jha, J.S.; Toppo, S.P.; Singh, R.; Tewari, A.; Mishra, S.K. Deformation Behavior of Ti-6Al-4V Microstructures under Uniaxial Loading: Equiaxed Vs. Transformed-β Microstructures. *Mater. Charact.* **2021**, *171*, 110780. [CrossRef]
48. Lütjering, G. Influence of Processing on Microstructure and Mechanical Properties of (A+β) Titanium Alloys. *Mater. Sci. Eng. A* **1998**, *243*, 32–45. [CrossRef]
49. *ASTM F3001-14(2021)*; Standard Specification for Additive Manufacturing — Titanium-6 Aluminum-4 Vanadium ELI (Extra Low Interstitial) with Powder Bed Fusion. ASTM International: West Conshohocken, PA, USA, 2014.
50. Xu, R.; Hu, X.; Yu, X.; Wan, S.; Wu, F.; Ouyang, J.; Deng, F. Micro-/Nano-Topography of Selective Laser Melting Titanium Enhances Adhesion and Proliferation and Regulates Adhesion-Related Gene Expressions of Human Gingival Fibroblasts and Human Gingival Epithelial Cells. *Int. J. Nanomed.* **2018**, *13*, 5045–5057. [CrossRef] [PubMed]
51. Levin, M.; Spiro, R.; Jain, H.; Falk, M.M. Effects of Titanium Implant Surface Topology on Bone Cell Attachment and Proliferation in Vitro. *Med. Devices Evid. Res.* **2022**, *15*, 103–119. [CrossRef]
52. *ISO 10993-5:2009*; Biological Evaluation of Medical Devices—Part 5: Tests for In Vitro Cytotoxicity. International Organization for Standardization: Geneva, Switzerland, 2009.
53. Hanawa, T. Biocompatibility of Titanium from the Viewpoint of Its Surface. *Sci. Technol. Adv. Mater.* **2022**, *23*, 457–472. [CrossRef] [PubMed]
54. Mei, S.; Yang, L.; Pan, Y.; Wang, D.; Wang, X.; Tang, T.; Wei, J. Influences of Tantalum Pentoxide and Surface Coarsening on Surface Roughness, Hydrophilicity, Surface Energy, Protein Adsorption and Cell Responses to PEEK Based Biocomposite. *Colloids Surf. B Biointerfaces* **2019**, *174*, 207–215. [CrossRef]
55. Chandar, S.; Kotian, R.; Madhyastha, P.; Kabekkodu, S.; Rao, P. In Vitro Evaluation of Cytotoxicity and Corrosion Behavior of Commercially Pure Titanium and Ti-6Al-4V Alloy for Dental Implants. *J. Indian Prosthodont. Soc.* **2017**, *17*, 35. [CrossRef] [PubMed]
56. Dohan Ehrenfest, D.M.; Coelho, P.G.; Kang, B.-S.; Sul, Y.-T.; Albrektsson, T. Classification of Osseointegrated Implant Surfaces: Materials, Chemistry and Topography. *Trends Biotechnol.* **2010**, *28*, 198–206. [CrossRef] [PubMed]

Disclaimer/Publisher's Note: The statements, opinions and data contained in all publications are solely those of the individual author(s) and contributor(s) and not of MDPI and/or the editor(s). MDPI and/or the editor(s) disclaim responsibility for any injury to people or property resulting from any ideas, methods, instructions or products referred to in the content.